The Century of Space Science

IV THE SIGNIFICANCE OF SPACE FOR FUNDAMENTAL SCIENCE

7. The Solar System

Earth Science –Oceanography

by

Johnny A. Johannessen, Stein Sandven, Dominique Durand

Phone: +47-55-297288, fax: +47-55-200050, email: johnny.johannessen@nrsc.no

Nansen Environmental and Remote Sensing Center

Edv. Griegsvei 3a, 5059 Bergen, NORWAY

7. The Solar System

Earth Science –Oceanography

by

Johnny A. Johannessen, Stein Sandven, Dominique Durand
Phone: +47-55-297288, fax: +47-55-200050, email: johnny.johannessen@nrsc.no

Nansen Environmental and Remote Sensing Center
Edv. Griegsvei 3a, 5059 Bergen, NORWAY

Table of Content.

ABSTRACT

Satellite oceanography began with the Gemini XII flight in November 1966. From a Hasselblad camera mounted in the pilot's window large internal waves in the eastern tropical Atlantic were photographed via sunglitter for the first time. The ability to observe and analyze the ocean surface from space has, since then, improved significantly thanks to the instrument technology development combined with advances in high performance computing and numerical simulation. Today Earth observing satellites provide global, quasi-synoptic, repetitive and homogeneous observations of a large number of geophysical and bio-chemical variables and processes at the ocean surface. Included among these are sea ice extent and concentration, sea surface temperature, sea level and ocean circulation, sea state and algae bloom. These observations are highly complementary to those data collected by in-situ sensors and form an essential element in the global ocean observing system. In this article, the status of satellite oceanography at the onset of the new millennium is assessed in the context of two categories, namely climate research and monitoring and operational oceanography. Looking ahead, the challenge and need to explore new Earth Observation capabilities aimed at bringing new data and scientific understanding is then discussed and recognized in light of the importance and demand to ensure continuity of existing satellite oceanography.

1. INTRODUCTION

At the onset of this new millennium increased awareness of the stresses being placed on the Earth system, often induced by human activities, has intensified the need for information on the present state of the Earth system and for enhanced capability to assess its evolution such as associated with environmental pollution, natural resource management, sustainable development, and global climate change.

This realisation has resulted in increased political and legal obligations on governments and national and regional agencies to address Earth system topics of global concern. These obligations are often encapsulated within international treaties, whose signatories have explicit requirements placed upon them

Many of these treaties call for systematic observations of the Earth to increase our understanding of its processes and our ability to monitor them:

- The UN Framework Convention on Climate Change (FCCC).
- The UN Convention to Combat Desertification in those Countries experiencing Serious Drought and/or Desertification.
- The Montreal Protocol of the Vienna Convention on the Protection of the Ozone Layer.
- Agenda 21 and the UN Commission on Sustainable Development.
- The Intergovernmental Panel on Climate Change.

These commitments require substantial economic, technical and scientific resources for their execution, and action at many levels, including significant programmes of global observations. In this context it is recognised that Earth observation satellites provide an important and unique source of

information. The most well established international forum for coordinating the operational provision of data is without doubt the World Weather Watch (WWW) of the World Meteorological Organisation (WMO). Another prominent, though less established forum is the Global Ocean Observing System (GOOS). Common for these international forum and observing system is the role of Earth Observation. Here it is worth mentioning the World Climate Research Program (WCRP), International Geopshere and Biosphere Program (IGBP) and Intergovermental Oceanographic Committee (IOC) in which research projects and observing systems highlight the importance of continuous and regular access to Earth Observation data.

Earth observations from satellite are highly complementary to those collected by in-situ systems. Whereas in-situ measurements are necessary for underwater observations, for high accuracy local observations, for the calibration of observations made by satellite and as input to models, satellite observations provide an inherent wide area unique capability to obtain regular quantitative information of surface variables and upper layer phenomenon at global, regional and local scales.

Present-day applications of satellite data are widespread and cover research, operational and commercial activities. These activities are of interest in the global context and the regional, national, and local context where Earth observation data are successfully applied in support of a range of different sectors, including (not exclusive):

- climate change research,
- stratospheric chemistry, particularly related to the ozone hole,
- weather forecasts based on Numerical Weather Prediction (NWP),
- agriculture and forestry services,
- resource mapping,
- hazard monitoring and disaster assessment,

- sea ice monitoring,
- coastal zone management,
- oceanographic applications

The number of Earth Observing satellites are growing rapidly for both scientific research and operational application within fields of land, atmosphere, marine meteorology and oceanography including sea ice covered regions. International investment in satellite platforms, instruments and associated ground segments is already substantial, and more investment is planned over the coming decade. There are currently over 45 missions operating, and around 70 more missions, carrying over 230 instruments, planned for operation during the next 15 years by the world's civil space agencies (CEOS, 97). In addition, Space Agencies are currently implementing their new strategy for defining future Earth Observing satellites, both dedicated research missions and continuous (operational) monitoring missions.

In this article we will review the status of satellite oceanography at the onset of the new millennium. In section 2 the principal methods, instruments and basic measured surface parameters are addressed. Examples of contribution to climate monitoring and operational oceanography are then given in section 3 and section 4, respectively. In section 5 an outlook towards the near future satellite observing system is provided followed by a summary in section 6.

2. PRINCIPAL METHODS, INSTRUMENTS AND SURFACE CHARACTERISTICS

Satellite oceanography is primarily using three domains within the electromagnetic (EM) spectrum, notably radiation in: - the visible/near-infrared (VNIR); - the thermal infrared (TIR); - and the microwave bands of the EM spectrum (Figure 1).

The visible and infrared channels utilize intervals of the EM spectrum with high atmospheric transmission, such as in the bands from 0.4 - 2.5 μm, 3.5 -4.0 μm and 10 - 13 μm (Fig. 1, top). The EM waves in these bands do not generally penetrate clouds, so remote-sensing observations of the Earth's surface in these bands can only be done satisfactorily under cloud free conditions. As such this is posing severe limitations in regions where clouds are frequently present. In the microwave area, on the other hand, at wavelengths above 0.3 cm, EM waves generally penetrate clouds which makes it feasible to obtain regular, daily observations of ocean and sea ice surfaces (Fig. 1, bottom). These characteristic spectral domains are further addressed in the following

2.1 Visible/Near Infrared

The basic quantity observed in the VNIR domain is the albedo or alternatively the fraction of the incident sunlight that has been scattered and/or reflected in the atmosphere/ocean system. The incident solar radiation undergoes a number of interactions (absorption and scattering) with molecules and particles in the atmosphere and in the water, in addition to the reflection that occurs at the air-sea interface.

Only a fraction of the incident radiation penetrates the water body. Absorption by water molecules becomes critical at wavelength greater than 700 nm (see Figure 1). Therefore water appears black at such wavelength, except when a high load of suspended sediment is present near the surface. The visible light (400 – 700 nm) may propagate in the water medium and interact with water molecules, organic and

inorganic particles in suspension, dissolved optically active substances, and possibly the sea-floor in optically shallow-waters. The penetration depth depends upon the wavelength and the water column absorption properties. Only a small fraction of the visible-light spectrum is scattered upwards to the surface giving rise to the so-called water-leaving radiance, L_w. This is expressed as:

$$L_w = (L_s - L_a - \alpha L_r)/\alpha \qquad (2.1)$$

where L_s is the radiance reaching the sensor, L_a is the atmospheric radiance, L_r is reflected radiation from the sea surface and α is the atmospheric diffuse transmittance. In most oceanic waters, L_w represents less than 10% of the total signal measured by a spaceborne sensor. Typically, 90 % of radiation has been scattered in the atmosphere, without interaction with subsurface waters. Therefore any quantitative estimation of water-column optically active constituents depends upon an adequate retrieval of the water-leaving radiance L_w emanating from the water column. This requires reliable correction of the remotely sensed signal scattered in the atmosphere and reflected at the air-sea interface (Gordon, 1997).

Furthermore the capability of deriving the accurate quantity of a particular water quality parameter depends upon the complexity of the water column in terms of number and properties of components that interact with the electromagnetic signal. According to the optical complexity of the water body, two types of water are defined, namely case I and case II waters (Morel and Prieur, 1977).

Case I waters are natural open-ocean water bodies, for which water-leaving radiance measured by remote sensors are only dependent on chlorophyll pigment concentration. In such waters, which represent around 90% of the World ocean, the variation in the color of the upper water column could be related to the variation of the concentration of chlorophyll pigments contained in phytoplankton cells. The color of oceanic case I waters shifts from deep blue in oligotrophic waters (very low chlorophyll concentration) to dark green in eutrophic waters (high concentration). This shift results from the strong absorption by algae

pigments (chlorophyll pigments and carotenoids) in the blue part of the visible spectrum, with a maximum around 445 nm, compared with the weak absorption around 550 – 580 nm (Morel, 1998). In case I type water, quite robust empirical relationships can be derived, linking the chlorophyll concentration to the ratio of water leaving radiance (and/or the reflectance of the sea) at these wavelengths.

Case II waters are more optically complex. In such waters the satellite derived water-leaving radiance, in addition to being dependent upon chlorophyll pigments and derived products, is also sensitive and modified by at least one other optically-active component, e.g., suspended sediment and/or colored dissolved organic matter. Most coastal waters are classified as case II waters. Furthermore the various optically active components do not display typical linear relationship. Therefore simple empirical models may no longer be used, and more sophisticated approach, such as inverse modeling must be considered.

2.2 Thermal Infrared

For TIR (and PMW) the measured quantity is the emitted energy as function of surface temperature and emissivity. The emissivity is a dimensionless coefficient, e, and can be computed from the complex dielectric constant (or the relative permettivity) $e = e' - i\,e''$, which characterizes the electrical properties of the media. e' is referred to as the dielectric constant and e'' as the dielectric loss factor. Alternatively, e can be estimated from the complex index of refraction such as $n^2 = e$.

In the thermal infrared part of the spectrum, the surface signal expressed as the radiance observed by remote sensing can be used as input to Planck's law of radiation to find the sea surface temperature (SST) if the emissivity e of the surface is known. For water, the value of e in the most used thermal spectral band of 10 μm -12 μm is very high and stable, about 0.99. At a given wavelength λ the blackbody radiance, L, can be expressed as:

$$L = \frac{\frac{2\Pi hc^2}{\lambda^5}}{e^{\frac{hc}{\lambda kSST}} - 1} \qquad (2.2)$$

In the thermal infrared domain, on the other hand, the Planck's law is usually expanded in a Taylor series from which the linear term is maintained:

$$Ln\,(L) = a\,T_b^{-1} + b \qquad (2.3)$$

where T_b is the brightness temperature in the TIR part of the spectrum, and the coefficients *a, b* are constant values for each spectral band.

2.3 Passive Microwaves

In the microwave domain the brightness temperature T_b provides the measurement of the microwave emission from the surface. The brightness temperature is defined by the real surface temperature T_s and the emissivity *e* by the relation

$$T_b = T_s * e \qquad (2.4)$$

Spatial variations in T_b observed over the surface of the Earth are due primarily to variations in the emissivity of the surface material and secondly to variations in surface temperature. For the most frequently used frequencies between about 6 GHz and 90 GHz, the emissivity of both ice and water show large variations allowing observations of a wide range of multidisciplinary parameters spanning land, ocean, cryosphere and atmosphere

While *e* for calm water can be calculated quite accurately from the electric properties (Stogryn, 1971), the value and variation of *e* for the various forms of ice and snow is less accurately known, and

therefore often has to be empirically measured. For sea ice, the dielectric constant *e'* is relatively constant with frequency above 1 MHz, but *e''* is not. There is a minimum in *e''* at 3 - 8 GHz with higher value for lower and higher frequencies.

For firstyear ice at 283 K and 8 ‰ salinity, the minimum *e''* is approximately 0.3. As temperature decreases *e''* will increase because precipitated salt will go back into solution. Furthermore, *e''* will decrease with decreasing salt content. Multiyear ice has a lower *e''* than firstyear ice and its temperature dependence is weaker. Thus, microwave radiation penetrates deeper into multiyear ice than firstyear ice.

2.4 Active Microwaves

Radar instruments provide their own source of illumination in the microwave portion of the EM spectrum, at wavelengths on the order of 10^4 longer than those in the visible part of the spectrum (Figure 1). Because of this, radars can operate independent of solar illumination, cloud cover and precipitation conditions.

All radar measurements can be described by a basic equation, which relates transmitted power, distance, reflectivity and antenna characteristics. The equation can be formulated as

$$P_R = \frac{P_t}{4\pi R^2} G \frac{\sigma}{4\pi R^2} A \qquad (2.5)$$

where P_R is power received, P_t is power transmitted, G is the gain of the antenna, σ is the radar cross section, and A is antenna area. The energy of the outward propagating wave, which is spherically expanding, is given by the first ratio. This spherically expanding wave is focused down to an angular beamwidth by the antenna so that the fluxes becomes higher by a factor of G over that of a spherically expanding wave. The focused energy impinges on an object which has a radar cross section σ, which is defined as the equivalent of a perfectly reflecting object of a given area which reflects isotropically

(spherically) as shown by the second ratio. Finally, the antenna area, *A*, term intercepts a portion of the reflected wave so that this portion of the flux defines the power received by the antenna.

The basic radar equation is general; it can be applied to any object of any shape or composition. For imaging over areas of terrain or ocean, a reflection coefficient is defined, σ_0, which is the radar cross section, σ, per unit area. The radar equation (2.5) can then be expressed as

$$P_R = \frac{\lambda^2}{(4\pi)^3}\int \frac{P_t G^2 \sigma_0}{R^4} dA \qquad (2.6)$$

The averaged received power for a radar can then be determined by examining the integral radar equation for distributed targets. The radar scattering coefficient, σ_0, also called backscatter coefficient, expresses a measure (usually in dB units) of the energy scattered back towards the antenna. It is a function of frequency, incidence angle, polarization and the scattering characteristics of the illuminated area.

Radar frequencies are identified by letter designations, and the most commonly used are K-band (30 GHz, 1 cm), X-band (9.4 GHz, 3.2 cm), C-band (5.3 GHz, 5.7 cm), L-band (1.25 GHz, 23.5 cm) and P-band (450 MHz, 62 cm). At these wavelengths the EM-waves are not appreciably attenuated by clouds, precipitation or the Earth's atmosphere (see Figure 1). Therefore, good quality radar data can be obtained during all kind of weather and light conditions. The three main classes of satellite radars (altimeter, synthetic aperture radar, and scatterometer) are further described in the following sections.

2.4.1 Radar Altimeter

The radar altimeter measures the transit time and backscatter power of individual transmitted pulses. The transit time is proportional to the satellite's altitude above the ocean, land or ice surfaces.

The pulse propagates toward the surface at time t_1 with a speed of light c, is backscattered by the surface, and an echo is received by the sensor at a time t_2. The time difference $t_d = t_2 - t_1$ is equal to the round trip distance to the reflecting surface divided by the propagation speed

$$t_d = 2h/c \tag{2.7}$$

The accuracy with which the distance h is measured is given by

$$\Delta h = \Delta c t_d/2 + c\, \Delta t_d/2 \tag{2.8}$$

The time difference accuracy $\Delta t_d/2$ depends mainly on the sharpness of the pulse which is equal to $1/B$ where B is the signal bandwidth (Elachi, 1987). Over ocean surfaces the measured range is accurate to better than 2.5 cm at al along track resolution of about 5 km. Higher range accuracy is achieved by detailed analysis of the received signal resulting from averaging a large number of echoes. Range errors and corrections may be associated with the instrument including the ultra-stable oscillator, and the environment such as the total electron content in the ionosphere, path delays within the atmosphere (dry and wet troposphere), and sea state bias. The latter results from the interaction of the altimeter's radar pulse with the sea surface. Simple parametric models are usually applied that express the sea state bias as a function of the wind speed and the significant wave height. The correction ranges between 0 to 20 cm and increases with wind speed and wave. As one typically lack precise knowledge of the wind speed and wave height along the altimeter ground track the sea state bias error is the major error source, and currently intensive investigations are conducted to develop more realistic models (Gaspar and Florens, 1998).

Over the ocean the magnitude and shape of the returned echoes also contain information about the characteristics of the reflecting surface, form which it is possible to retrieve geophysical parameters such as significant wave height, wind speed and sea ice edge location.

2.4.2 Synthetic Aperture Radar

The synthetic aperture radar (SAR) is a side-looking radar that forms an image by a series of electromagnetic pulses transmitted towards the Earth in a direction perpendicular to the satellite track and reflected back towards the antenna. As the incidence angle of a SAR is oblique to the local mean angle of the ocean surface, there is almost no direct specular reflection except at very high sea states in near range. It is therefore assumed that at first approximation Bragg resonance between the radar and ocean waves is the primary mechanism for backscattering radar pulses (Wright, 1978; Elachi, 1987). The Bragg equation is defined as:

$$\lambda_r = 2\ \lambda_s\ sin\theta \qquad (2.9)$$

where λ_r is the radar wavelength, λ_S is the sea surface wavelength and θ is the local angle of incidence. These short capillary-gravity waves at the Bragg-scale form in response to the wind stress and are further modulated by the longer waves.

Range is used to define the location of an object in the cross-track direction, which is perpendicular to the satellite flight direction, while azimuth defines the location in the along track direction. In imaging theory, *resolution* of a radar system is defined as the radar's ability to discriminate between two point targets, observable as bright spots in a particular image. Two different principles determine the resolution of a radar system: Azimuth resolution is defined by the beamwidth β of the radar, which is the angle by

which the radar beam expands and is a function of the antenna size and range. The along track dimension, or azimuth resolution r_a is defined as

$$r_a = R\beta \qquad (2.10)$$

where R is the range distance to the illuminated object. The beamwidth of the radar is a function of the antenna length (D), with larger antenna producing a narrower beam. For a real aperture radar, such as SLAR, the only way to obtain fine azimuth resolution is to have a very short range or a very large antenna. Synthetic Aperture Radars (SAR) overcomes this problem by utilizing the Doppler shift induced by the along-track motion of the satellite (or aircraft) to simulate a very large antenna. The finest possible azimuth resolution is therefore approximated by:

$$r_a = D/2 \qquad (2.11)$$

The unique advantage of the SAR sensor is therefore that the azimuth resolution (in the order of 10 m) is independent of the range and the platform altitude.

The range resolution r_r of a radar system is

$$r_r = ct_p/(2\sin\theta) = c/2B\sin\theta \qquad (2.12)$$

where t_p is the equivalent length of the transmitted radar pulse, c the speed of light, θ the incidence angle and B the pulse bandwidth. The range resolution is therefore corresponding to the minimum distance two objects must be separated to be detected by the SAR at these two unique ranges.

Imaging radars operate in the microwave frequencies between 400 MHz and 35.2 GHz, corresponding to wavelengths between 62 and 0.85 cm. As the bandwidth, $B = 1/t_p$ of the SAR transmitted signal pulses is large it is therefore possible to obtain a fine resolution (in the order of 10 m) in range. Note that this is achieved by modulating the transmitted pulse to obtain a short pulse length.

Another characteristic feature of imaging radar systems is polarization, which is defined as the direction of the electric vector of an EM wave. The electric vector is the plane in which the EM energy is transmitted. Visible light is unpolarized because the direction of the electric vector is randomly distributed. For radar systems it is common to emit pulses, which are either horizontally (H) or vertically (V), polarized. The radar antenna can receive either the horizontally- or vertically-oriented return signal, or both. Extensive description of radar remote sensing principles are found in Ulaby *et al*. (1982 a, b) and Elachi (1987).

2.4.3 Scatterometer

Side looking scatterometers acquire wide swath coverage along the side of the satellite sub-track. Every strip at a distance y from the sub-track is observed at an incidence angle θ given by (neglecting the curvature of the Earth)

$$\theta = tan^{-1}\ (y/h) \qquad (2.13)$$

where h is the height of the satellite above the sub-track. The measurement principal is in general identical to the case of a real aperture imaging radar. With a fan-shaped beam the covered swath corresponds to the range footprint of the antenna. The azimuth resolution X_a is defined by the azimuth footprint, and the range resolution X_r by the pulse surface footprint.

In contrast to the imaging SAR, scatterometers typically provide coarse resolution observations in the order of 50 km. Neither Doppler shift to obtain fine resolution in azimuth nor pulse modulation to

obtain large bandwidth and hence gain fine range resolution are utilized as resolution is considered of secondary importance to the radiometric accuracy and extent of coverage.

In addition to the side looking configuration, scatterometers can be forward (or backward) looking, squint looking, or they can use pencil beam circular scanning principles. Hitherto the most common spaceborne scatterometers have used a combination of side looking and forward (backward) looking configurations (e.g. ERS scatterometer, and NSCAT). In so doing the wide swath capability (~500 km) is combined with the ability to observe the surface from different look directions. In turn, the angular signature (azimuthal behavior) of the surface scattering elements is acquired.

2.5 Parameter Retrieval Summary

From the electromagnetic measurements within these frequency domains and associated bands one can in turn derive a set of key physical and bio-chemical variables and fields based on dedicated retrieval algorithms. They include SST, surface roughness, sea surface height (or slope), sea ice field and so-called ocean color. As shown in Table 1 they can be further broken down into a large number of quantities in which the sea ice field can be related to ice extent, concentration, type and motion, and sea ice edge features; surface roughness in different ways can be related to near surface vector wind, wind speed, wave spectra, significant wave-height, and surface current features, surface height can be related to surface geostrophic current and mean sea level, and ocean color or water leaving radiance can be related to chlorophyll concentration.

The most common satellite instrument used for measuring in the VNIR and TIR domains is the Advanced Very High Resolution Radiometer (AVHRR) which provide images with spatial resolution of about 1 km in 3-5 different frequency channels. Passive microwave (PMW) radiometers, such as SSM/I, observe in a similar manner the emitted radiation in the microwave domain at different wavelengths and polarizations. The ground resolution of PMW instruments varies in the range from 10 to 50 km, depending on the choice of frequency (or wavelength). Active microwave (AMW) observations can be

classified in several types of instruments including synthetic aperture radars (SAR), side-looking radars (SLAR), scatterometers and radar altimeters. Whereas the three first AMWs are illuminating the surface at incidence angles typically varying from 20 to 50 the latter is nadir looking. The SAR instruments provide high resolution images, with pixel size down to about 10 m, while spaceborne SLARs provide medium resolution images with resolution of 1 - 2 km. Scatterometer data have coarser resolution, varying from 10 km to about 50 km. Radar altimeters, on the other hand, are profiling the surface along the satellite ground track with a resolution of the order of 3-5 km.

A list of the most common satellites (past, present and future) and instruments of the classes presented above is provided in Annex B together with some relevant sensor and satellite characteristics such as swath width, spatial resolution, and launch date. In addition, Figures A1 and A2 provide a timeline of the most common VNIR/TIR and PMW/AMW sensors for oceanography operated in space since 1972 together with those approved and planned towards 2010.

Although there is some degree of overlap between the observed quantities and sensor types as indicated in Table 1 they are of complementary nature rather than redundant. In many cases this synergy of different sensors are allowing more reliable retrievals than otherwise would be the situation.

The separation into the three different classes, notably: C – climate monitoring, OP – operational and R – research is furthermore illustrating the multi-purpose use of the data in which, for instance, a derived quantity can be applied in a operational service and in parallel be used in research.

The scope of the paper is not to give a complete and comprehensive review of satellite oceanography within all the classes identified in the Table 1. In the remaining of the paper we will, on the other hand, address the satellite retrieval capabilities and application in the context of Climate Research and Monitoring in section 3 and Operational Oceanography in section 4. An overview of the

near future satellite observing system is then provided in section 5 followed by the Summary in section 6.

3. CLIMATE RESEARCH AND MONITORING

The past decade has seen increasing public concern about the Earth, its environment and mankind's impact upon it. Global threats such as climate warming, stratospheric ozone depletion, tropospheric pollution and more recent regional events such as the very intense El Niño, the fires in the S.E. Asia and the floods in many parts of the world have left public more concerned than ever about the need both to monitor and understand the Earth's environment.

At international level, agreements and treaties are signed by many countries encompassing climate change issues and at the highest level the Intergovernmental Panel on Climate Change (IPCC) was established under the auspices of the United Nations to advise governments on climate change and its implications. Priority issues, as identified by IPCC, are:

- sources, sinks and concentration of greenhouse gases,
- the Earth radiation balance,
- effect of ocean circulation on the timing and pattern of climate change,
- hydrological cycle
- polar ice sheets, freshwater and changing sea level
- ecosystem dynamics,
- large scale insertion of aerosols into the atmosphere

Ultimately, our understanding of the Earth will improve by the development and elaboration of Earth system models into which data from various sources will be integrated. In view of satellite observations in oceanography this is further discussed in the context of sea ice, sea surface temperature, sea level and ocean circulation and carbon cycle. Details of the outstanding scientific advances made possible by satellite observations of the ocean and the associated societal benefits

are provided by Halpern (2000). Note also that a comprehensive overview of the new era for oceanography where the core needs for an integrated, coordinated and sustained global ocean observing system for climate and related physical oceanographic issues of research and of operational applications are provided by Smith and Koblinsky (2001).

3.1 Sea Ice

Sea ice is defined as any ice which is formed as a result of freezing of sea water. Sea ice occurs at the surface of the ocean in areas where the surface temperature is cooled to the freezing point which is about –1.8 ° C for sea water with salinity of about 35 parts per thousand (ppt).

Sea ice is a part of the cryosphere which interacts continuously with the underlying oceans and the atmosphere above. The growth and decay of sea ice occur on a seasonal cycle at the surface of the ocean at high latitudes. As much as 30 mill. km^2 of the Earth's surface can be covered by sea ice. In the Northern Hemisphere, sea ice extent (area enclosed by the ice boundary) fluctuates each year from a minimum in September, when most of the ice is confined to the central Arctic Ocean, Greenland Sea and Canadian Archipelago, to a maximum in March, when the sea ice covers almost the entire Arctic Ocean and many adjacent seas. In the Southern Hemisphere, the annual fluctuation is even greater, from a minimum in February to a maximum in September when the ice surrounds the Antarctic continent and extends equatorward to 55° - 65° S (Gloersen *et al*., 1992). Figure 2 shows example of maximum and minimum ice extent observed by passive microwave satellite data.

The largest volume of sea ice is found in the Northern Hemisphere in March, 0.05 mill km^3, which is nearly twice the maximum sea ice volume in the Southern Hemisphere. The reason for this is the mean thickness of the Arctic sea ice which is about 3 m, whereas the mean thickness of the Antarctic sea ice is 1 - 1.5 m.

Sea ice has many roles in the global climate system. For one, it serves as an effective insulator between the ocean and the atmosphere, restricting exchange of heat, mass, momentum and chemical constituents. During winter when there is large temperature difference between the cold atmosphere and the relatively warm ocean surface, ocean-to-atmosphere heat transfer is essentially limited to areas of open water and thin ice within the pack. The winter flux of oceanic heat to the atmosphere from open water can be two orders of magnitude larger than the heat flux through an adjacent thick ice cover. As a result, the distribution of open water and thin ice is particularly important to the regional heat balance.

Another important role of sea ice in the global climate system is that it affects surface albedo. Ice-free ocean generally has albedo below 10 - 15 %, whereas snow-covered sea ice albedo average to about 80 %. A fresh snow cover on the ice can increase the surface albedo to values as high as 98 %, whereas melt ponds can decrease the ice albedo to as low as 20 %. Because the albedo of snow-covered sea ice is high, relative to that of open water, the presence of sea ice considerably reduces the amount of solar radiation absorbed at the Earth's surface. This is most significant in summer, when the insolation, or solar heating is high.

Sea ice processes also affect oceanic circulation directly by the rejection of salt to the underlying ocean during ice growth. This increases the density of the water directly under the ice, thereby inducing convection that tends to deepen the mixed layer. This convection contributes to driving the thermohaline circulation of the ocean. In regions with density structures that were initially weak or unstable, this can lead to overturning and deep water formation. Much of the world oceans' deep and bottom water is formed in polar regions by these mechanisms. Conversely, the input of relatively fresh water to the ocean during ice melt periods tends to increase the stability of the upper layer of the ocean, inhibiting convection. Furthermore, the net equator-ward transport of ice in each hemisphere produces a positive freshwater transport and a negative heat transport.

The first satellite sensors providing views of the large-scale structure and motion of sea ice utilized visible and infrared channels such as those onboard the early Nimbus, Tiros, and Earth Resources and Technology Satellite (ERTS, later renamed Landsat). By the late 1960s, it was apparent that the sequential synoptic observations needed for sea ice and climate studies could not be acquired by satellite-borne visible sensors, which are limited to cloud-free and well-illuminated conditions. Sea ice exists in regions which are dark for several months and are frequently cloudy in the remaining months (Gloersen *et al*., 1992).

Therefore, it has been necessary to develop observation methods using microwaves which are able to penetrate clouds and are not dependent on light conditions. The first passive microwave remote sensing systems for satellites were launched on the Russian Cosmos 243 and Cosmos 384 in 1968 and 1970, respectively. In the US, passive microwave technology was first used in remote sensing of sea ice during the late 1960s and early 1970s, when a prototype of the Electrically Scanning Microwave Radiometer (ESMR) was flown on Nimbus-5 over the Arctic (Campbell, 1973).

The period since 1970 has been one of great advancement in remote sensing of sea ice. After the ESMR period 1973 - 1976, a more advanced satellite instrument, the Scanning Multichannel Microwave Radiometer (SMMR) was operated on Nimbus-7 for nine years, from 1978 to 1987. Together with the DMSP SSM/I, which has been the "working horse" since 1987, the longest and most regular time series of global sea ice data has been provided at a resolution of typically 30 km .

In 1978, Seasat was the first satellite which provided high resolution SAR images of sea ice, but the satellite only operated for about three months. With spaceborne SAR data, which combines high spatial resolution with independence of cloud cover and light conditions, it is possible to observe sea ice with much better accuracy than visible and passive microwave methods. ERS-1 represented a major milestone in satellite SAR remote sensing of sea ice, because the satellite delivered tens of thousands of SAR

images of sea ice from most ice covered regions in the world. The satellite SAR technology is being improved and SAR systems offered by the Canadian RADARSAT and the European ENVISAT satellites have wide swath, multimode, dual polarization. Also other microwave systems such as scatterometer and side-looking radar (SLR) data have shown promising results in sea ice observations (Gohin and Cavanie., 1994; Grandel *et al*.,1999).

Today, data from polar orbiting satellites are used extensively in research as well as monitoring of sea ice extent and other relevant ice parameters (Johannessen *et al*., 1992, 1995; Carsey *et al*., 1992). As general coupled atmosphere-ocean circulation models predict enhanced climatic warming in polar areas, it is expected that this should be reflected in reduced ice extent and concentration, a decreased mean sea ice thickness as well as possible changes in the intensity and number of pressure ridges. The regular use of satellite data is therefore also essential for model validation.

The microwave brightness temperature T_b of the Earth's surface depends on the electrical properties of the surface, embodied in its emissivity e and the physical temperature of the radiating portion of the surface T_s. From eq. 2.4, this may be expressed by the following relation in terms of the wavelength λ and polarization p:

$$T_b [\lambda, p] = e[\lambda, p] T_s \qquad (3.1)$$

This relationship is true only for e and T_s independent of depth, a typical assumption for sea ice (Steffen, *et al*., 1992). The radiative transfer equation is the basis for the development of algorithms that convert the satellite radiance data into geophysical parameters. The microwave radiances received by the satellite are composed of various contributions from the Earth, atmosphere and space. The radiation received by the satellite, which is a function of wavelength and polarization, can be expressed by the equation:

$$T_b = e\, T_s\, e^{-\tau} + T_{up} + (1\text{-}e) T_{down}\, e^{-\tau} + (1\text{-}e)\, T_{sp}\, e^{-2\tau} \quad (3.2)$$

where T_b , T_s e are as before, and $e^{-\tau}$ represents atmospheric absorption, T_{up} is the atmospheric upwelling radiation, T_{down} is the atmospheric downwelling component, and T_{sp} is the cosmic background component.

There are several well documented algorithms for estimation of sea ice concentration based on brightness temperature observed in several frequencies and polarizations as suggested in Figure 3 (Steffen *et al*., 1992). Among the most common retrieval algorithms we can note the NASA team algorithm (Cavalieri *et al*., 1984), the Bootstrap algorithm (Comiso, 1986), and the NORSEX algorithm (Svendsen *et al*., 1983).

Analyses shows that the actual differences between these algorithms are in general small. In the following discussion we have chosen to use the NORSEX algorithm, which was developed after the NORSEX marginal ice zone experiment near Svalbard in 1979 conducted by the NORSEX Group (1983). The algorithm computes area concentration of total ice and two ice types: multiyear ice (MY) and first-year ice (FY) using the 18 GHz and 37 GHz vertical polarization at a spatial resolution of 60 km.

An extension of the NORSEX algorithm (Svendsen *et al*., 1987) takes advantage of the improved spatial resolution of the 85 GHz channels provided by the SSMI system which is currently in operation. The 85 GHz channel, H polarization, (85H) is very sensitive to the difference between water and FY-ice as well as to the atmosphere. This channel is therefore used to sharpen the ice-water boundary.

Analysis of SMMR and SSM/I records taken separately revealed a greater reduction in Arctic sea ice area and extent during the SSM/I period as shown in Figure 4. The decreases from 1987-94 were ~4%

per decade compared to ~2.5% per decade from 1978-87 (Johannessen *et al.*, 1995), with no significant trends found in the Antarctic. Since then, merged SMMR-SSM/I time series have been produced and analyzed, establishing the trends more firmly. Bjørgo *et al.* (1997) showed that the trend in Arctic ice area and extent (1978-95) is about -0.3 x 10^6 km^2 per decade (Fig. 4 a and b), corresponding to ~3% per decade. The 3% per decade decrease in the Arctic ice extent (1978-97) was subsequently corroborated in a separate analysis (Cavalieri *et al.*, 1997) that also confirmed the hemispheric asymmetry seen earlier (Johannessen *et al.*, 1995; Bjørgo *et al.*, 1997). Cavalieri *et al.* (1997) found a slight (~1.5%) increase in the Antarctic, which may be considered significant. The hemispheric ice covers fluctuate quasi-periodically, with predominant periods between 3-5 years, though their variability is apparently not correlated (Cavalieri *et al.*, 1997).

The capability to monitor interannual variations in multi-year ice area from SMMR and SSM/I data has recently been exploited using winter data, when first-year and multi-year ice signatures permit their distinction (Johannessen *et al.*, 1999). The analysis revealed a relatively large (~7% per decade) reduction in the multi-year ice area 1978-98 (Figure 4 c), compared with an ~2% per decade decrease in the total ice area in winter. This finding is supported by a SMMR-SSM/I data analysis that found an 8% increase (5.3 days) in the length of the sea ice melt season in the Arctic from 1978-96 (Smith, 1998). It is also corroborated by spatially- and temporally-fragmentary observations (from submarine sonar transects) of ice thickness decreases, as well as oceanographic data that have revealed changes in Arctic water masses since the 1970s that are reasoned to stem from a substantial (~2 m) melting of perennial MY ice. If this trend were to continue, it could eventually lead to a markedly different sea ice regime in the Arctic, altering heat and mass exchanges as well as ocean stratification.

3.2 Sea Surface Temperature

Knowledge of the ocean's central role in modifying climate, through its large heat capacity and transport of properties coupled with its complex interactions with the atmosphere and cryosphere, has long been insufficient for the accurate prediction of climate change resulting from fluctuations in natural

or anthropogenic forcing. For example, it is known qualitatively that a large part of the excess energy input (the incoming solar radiation minus the infrared radiation to space) in tropical areas is carried by the oceans towards the poles, the other half being transported by the atmosphere (Peixoto 92). However, quantitative estimates are coarse, and predictions of how such fluxes would be modified by 'enhanced greenhouse forcing' are even more uncertain. Such uncertainties resulted in the formation of the World Climate Research Programme (WCRP) by the World Meteorological Organisation and the International Council of Scientific Unions and have been and are being addressed through very large oceanographic research programmes like WOCE and CLIVAR.

The monitoring of sea-surface temperature (SST) from Earth-orbiting infrared radiometers is the technique of marine remote sensing which has had the widest impact on oceanographic science (Robinson, 1985). The Advanced very High Resolution Radiometer (AVHRR) was first flown on TIROS-N in 1978, replacing the limited VHRR, which flew on the five first NOAA orbiting platforms. AVHRR can be seen as the first operational sensor for oceanography. Since 1978, there is always at least one functioning satellite in orbit, but the nominal configuration is two satellites working, in sun-synchronous orbits, separated by about 90^{o} of longitude, so that one gives a morning and the other an afternoon daytime overpass at each location with a spatial resolution at nadir of 1 * 1 km. AVHRR is also part of the METOP/EPS payload as approved by Eumetsat Council in June 1996.

A list of TIROS -NOAA satellites carrying AVHRR are given in Table 2. The Geostationary Meteorological Satellite (GMS) programme also provides infrared imagery of the oceans, primarily covering low- and mid latitudes, with a spatial resolution at nadir of 5 * 5 km and a repeat sampling capability of 30-minutes. The GMS programme is a world-wide co-operation which includes the American satellite series GOES and the European series Meteosat.

The most popular algorithm for surface temperature retrieval from TIR sensor is based on the so-called Split-window method, which use two bands in the thermal infrared for correcting for varying atmospheric emission and transmission. This type of algorithm is fully operational and used with both NOAA-AVHRR and ERS-ATSR data.

The basic equation as given by McClain *et al*. (1985) is:

$$SST = a*T4 + b_1*(T4 - T5) + c + b2*(T4-T5)*(\sec(\theta)-1) + c \qquad (3.3)$$

where a=1.02015, b_1=2.32, b_2=0.489, c= -278.52, and θ is the scan angle: The sea surface temperature is given in degree Celsius.

By linear combination of brightness temperature *T4* of channel 4 (10-11μm) and *T5* of channel 5 (11 -12μm) on AVHRR, the effect of varying atmospheric emission and transmission is largely removed.

Since moored buoys have been used to calibrate the algorithm effects of water emission coefficient and skin-to-bulk water temperature gradient can also been reduced or eliminated. The given coefficients are used globally for routine processing at NESDIS for daytime passes of NOAA-11. Slightly different values are used for night-time passes, and for instruments on other NOAA satellites. A distinction between ascending and descending pass data is often made, due to systematic differences in the algorithm and quality of day and night data, the night data being generally considered as the most accurate (less effect of the skin-temperature). Note that some instruments do not have split channels and as for Landsat-TM band 6, one are restricted to use single band algorithms

Satellite infrared imagery play a major role in the study of horizontal structures in sea surface temperature thanks to its large coverage at fairly good resolution (~1 km) during cloud free conditions.

In particular, these SST measurements are applied for many different purposes related to climate studies. Applications concern for instance the tracking of long-term global changes in SST related to natural short term variation of the climate system and/or to man-induced changes in the composition of the atmosphere (greenhouse effect).

In Figure 5 the monthly mean sea surface temperature (SST) differences between July 1995 and July 1997 derived from ERS-2 Along Track Scanning Radiometer (ATSR) is shown. Clearly noticed is the SST expression of the 1997 El Niño with a positive sea surface temperature anomaly (with regards to the July 1995 situation) exceeding 5˚ C in the eastern region. El Niño is a disruption of the ocean-atmosphere system in the tropical Pacific, which affects weather around the globe. The 1997-1998 El Niño is one of the strongest encountered in the last century causing destructive flooding in the US and Peru, and severe drought in the western Pacific, also associated with devastating fires. The phenomenon is characterised by a rise in the sea level (up to ~40 cm) and in the sea surface temperature (up to 8˚ C) in the eastern tropical Pacific. Such data are also important in research on equatorial dynamics and instability waves such as equatorial trapped large scale Kelvin waves and westward propagating Rossby waves. The interplay of these wave systems is considered to be important elements of the El Niño Southern Oscillation (ENSO). Further discussion of the sea level anomaly associated with the 1997-1998 El Niño is found in the next section.

As part of the ongoing 'AVHRR Oceans Pathfinder' project, NASA-JPL is tasked with reprocessing AVHRR to produce an accurate SST database especially suited for global climate studies (http://podaac.jpl.nasa.gov/order/order_avhrr.html). New processing procedures are used to improve the calibration accuracy and the number of valid retrievals (based on a quality flag). Weekly averaged data sets between November 1981 and August 1999 for both ascending (daytime) and descending (nighttime) orbits, are available on equal-angle latitude-longitude grids of 18 km squares at equator. An example of such a SST map is shown in Figure 6.

As well as playing a crucial role for the upper ocean thermal conditions the SST is also of fundamental importance in coupling the atmosphere and ocean. The skin of the ocean provides the lower boundary condition for the upwelling infrared radiation in the marine atmosphere. The air-sea temperature difference is a controlling factor in the exchange of heat and moisture (evaporation), and also determines the marine boundary layer stability, which has consequences on the air-sea fluxes of heat and momentum. The surface skin of the ocean is usually colder, by a few tenths of a degree, than the underlying bulk temperature of the water. This is due to the flow of heat from the ocean to the atmosphere by molecular processes through the upper millimeter or so of the water where turbulent transfer is suppressed by the density difference across the interface (Emery *et al*., 1995).

Satellite infrared (TIR) SST retrievals have two significant limitations:- proper retrievals cannot be obtained in cloudy conditions; and – atmospheric aerosols from volcanic eruptions and large fires can lead to significant cooling in the SST retrievals (Reynolds , 1993). As indicated in Table 1, on the other hand, passive microwave radiometry can offer a solution to the cloud and aerosol problem, provided the operating frequency is below 12 GHz (Wentz *et al*., 2000). In that frequency domain the surface radiance is proportional to SST and the microwaves penetrate clouds with little attenuation as was demonstrated with the PMW operated on Seasat and Nimbus-7. Moreover, the impact on the brightness temperature from atmospheric aerosols can be ignored. The usefulness of the early radiometers was, however, limited by poor calibration and large spatial resolution (~150 km).

The Tropical Rainfall Measuring Mission (TRMM), launched in November 1997, operates the TRMM microwave imager (TMI) with frequencies ranging from 10.7 to 85 GHz. As the orbit inclination is only 30˚ it offers no global coverage, but nevertheless, its data collected in the tropical oceans have shown very promising results (Wentz *et al*., 2000). Comparing their daily SST retrievals with buoy data

they obtained a root mean square (rms) difference ranging from 0.5˚ to 0.7˚ C. This difference is expected to be further reduced after more careful removal of retrieval errors and skin-to-buoy correction.

The TMI is the first in a series of satellite microwave radiometers. Within two years the Advanced Microwave Scanning Radiometer (AMSR) will also be operated on both a US and Japanese spacecraft. The AMSR will even have a additional channel at 6.9 GHz that will further enhance the SST retrieval.

3.3 Sea Level and Ocean Circulation

Sea-level change is one of the most important components of global climate research. Global-averaged sea-levels are considered to have risen by between 10 and 25 cm during the past century, and are predicted to rise by the order of half a meter in the next century (Warrick *et al*., 1996). This will have important consequences for the 50-70% of the World's population that lives within coastal zones, which depend on the agricultural and industrial productivity of coastal regions, or which have to be protected from coastal flooding (Bijlsma *et al*., 1996). Possible impacts on low-elevation coral islands (e.g. Maldives) and river deltas (e.g. Bangladesh) are obvious and have been well documented. Less well known is the fact that a rise of 50 cm along the coast of England and other parts of the European Atlantic coast will increase the probability of flooding by an order of magnitude (Coles and Tawb, 1990).

It is a challenge to come up with a full explanation for the sea level changes that has taken place in the 20th century since a number of competing geophysical processes, each of which is a complex process in itself, are contributing. Among these are interior Earth tectonics; the redistribution of water from ice sheet and glacier retreat; the rebound of the lithosphere and mantle and the affect of these on the Earth's gravity field; the thermal expansion of the oceans; the extraction of ground water; and changes in coastal sedimentation and erosion. The largest potential source is, nonetheless, the cryosphere. The rise in the 20th century corresponds to approximately 0.2% of the Antarctic Ice Sheet mass. However, little is known about the magnitudes of fluctuations in the ice sheets on this time-scale. In comparison, it appears that glacier retreat in Europe and North America may explain 4 cm of the present rise (Meier 84),

whereas the thermal expansion of the ocean associated with global warming is also estimated to have contributed perhaps 4 cm during the last century.

Measurements of sea level are made from space via satellite radar altimetry and from in-situ devices such as coastal tide gauges, bottom pressure recorders and GPS-buoy systems. During the last decade, the technique of radar altimetry has become fully developed, enabling routine and precise, quasi-global measurements of mean sea level to be obtained. Analyses of almost four years of TOPEX/POSEIDON altimetric data have provided observations of the ocean dynamic topography to an absolute accuracy of 3-4 cm. In comparison, the ERS-1 orbits are typically accurate to within 15 cm. However, since TOPEX/POSEIDON and ERS-1 were flying simultaneously, the more precise TOPEX/POSEIDON data can be used to correct the ERS-1 orbit error as shown in Figure 7. The same is possible for ERS-2, but with the improved orbit determination from the PRARE (Precise Range and Range-Rate Equipment) the differences are less (Le Traon and Ogor, 1998).

These programmes rely heavily on the availability of satellite altimetry data, such as provided by the TOPEX/POSEIDON and ERS-1/ERS-2 missions; operating simultaneously, these satellites allow the measurement of very precise, regular and quasi-global sea surface heights. As most changes in ocean surface currents (on timescales of a few days or longer) result in geostrophic balance, gradients of the sea surface pressure (or 'dynamic topography', the sea level above the geoid) as derived from radar altimetry can be employed almost directly as proxies for surface current information. Unlike in-situ measurements, they are global, synoptic and can be repeated for many years.

To advance our knowledge and prediction capabilities of the world climate at seasonal, interannual, and longer time scales, it is essential that ocean circulation processes be well observed, understood and simulated. Ocean thermodynamics has a stabilizing role on climate. The ocean and atmosphere together are responsible for the meridional heat transfers. Mechanical energy, mass and heat are exchanged at their

interface and couple the two systems together. Therefore global, repeated, observations of the ocean topography are a critical element of the research on climate dynamics and on the perturbations to the coupled atmosphere/ocean system.

On basin to global scales, the primary application is climate monitoring. This includes phenomena such as the El Niño Southern Oscillation which is manifested in sea surface temperature and sea surface topography anomalies (Figures 5 and 8) which occurs on seasonal to inter-annual time scales. These observations are very complementary and as pointed out in the discussion of Table 1 they advance the interpretation and reliability of the data. For monitoring such large-scale features, the timeliness of the altimetric analyses can be relaxed to a few weeks. On the other hand, it is critical to have the most accurate orbit available in that time-frame in order to secure a height estimate with an accuracy of no less than a few cm.

It is not possible to optimize the sampling of any single satellite mission to observe all oceanic processes and regions. The sampling problem must therefore be thought of in terms of coincident access to a set of complementary altimetric missions such as the overlapping of ERS-1/2 on a 35-day, sun-synchronous, polar orbit and the 10-day orbit of TOPEX/POSEIDON. There is a large improvement in sampling characteristics when going from one satellite to two satellites. Compared to TOPEX/POSEIDON, the combination of TOPEX/POSEIDON and ERS has, for example, a sea level mean mesoscale mapping error reduced by a factor of 4 and a standard deviation reduced by a factor of 5. The improvement in mesoscale sea level mapping is not as large when going from two to three or three to four satellites (Le Traon and Dibarboure, 1999).

On the other hand, they furthermore demonstrate that the mesoscale velocity field mapping is more demanding, in terms of sampling. The meridional and zonal mean velocity mapping errors are two to four times larger than the mesoscale sea level mapping error. The contribution from a third satellite

altimeter is also more significant as only a combination of three satellites can actually provide a velocity field mapping error below 10% of the signal variance.

In summary, these results confirms what is generally agreed as being the main requirement for future altimeter missions, i.e. that at least two (and preferably three) missions are needed with one very precise long-term altimeter system (such as T/P and later on Jason-1) to provide a reference for the other altimeter missions such as ERS, GEOSAT, and ENVISAT.

3.4 Carbon Cycle and the biological pump

It is generally acknowledged that marine biochemical processes, and particularly the carbon cycle in the ocean, contribute to global climate variability and changes. The natural buffering capacity of the world-ocean with respect to carbon has a direct implication of the atmospheric concentration of carbon dioxide – CO_2, which is considered as the most important greenhouse gas in the atmosphere. It is commonly agreed that the world-ocean takes up as much as 2 Gt of carbon per year (Denman *et al.*, 1996), hence contributing in the global decrease of atmospheric CO_2 of about 50%. The so-called biological pump is nowadays recognized as an essential component of the mechanisms of CO_2 exchange between the atmosphere and the upper ocean. Denman *et al.*(1996) report that the atmospheric concentration of CO_2 would have been 450 ppmv in absence of marine biota, instead of the current 280 ppmv.

Regarding this, satellite ocean color may provide valuable information on the state of the biological pump through the regular monitoring of chlorophyll pigment concentration as a proxy of phytoplankton biomass and primary production at global scale.

NIMBUS-7 (launched on 24 October 1978) operated, in addition to the SMMR, the Coastal Zone Color Scanner (CZCS); the first sensor specifically designed for ocean color surveillance. The CZCS was a scanning radiometer with five spectral bands at 443, 520, 550, 670, and 750 nm in the visible and NIR

range, and a sixth thermal infrared band at 10.5-12.5 μm. The NIMBUS-7 orbit was placed at a height of 995 km, giving the CZCS a ground resolution at nadir of 825 * 825 m. It ceased operating after eight years in 1986. During this period, CZCS recorded approximately 250,000 minutes of data (about 125,000 two-minutes scenes) demonstrating that satellite ocean color sensing provide an invaluable data set for synoptic monitoring of open-ocean biochemical processes, in particular associated with chlorophyll concentration and distribution in the upper ocean.

After a data gap of about ten years a new generation of increasingly-sophisticated VNIR and imaging spectrometers has been developed including MOS, OCTS, POLDER, and SeaWiFS launched in 1996-1997, MODIS, MISR, OCM, OCI, OSMI launched in 1999, and, GLI, POLDER-2 and MERIS scheduled to be launched in 2000 – 2001 (See Annex B). Presently more than six ocean color sensors are in operation. The instrument development and improvement have mainly consisted in better radiometric performances and increased number of spectral bands (from 5 for CZCS up to 36 for MODIS and GLI) (Morel, 1998). Other technological advancement have consisted in the introduction of multi-angle viewing capability (POLDER, MISR) and determination of the state of polarization of the reflected radiation (POLDER 1 and 2). In the past 5 years the ocean color sensing mission status have shifted from experimental or scientific research missions to pre-operational demonstration missions.

As mentioned already in chapter 2 two main challenges are related to the processing of ocean-color data, namely: 1) atmospheric correction, and 2) the need to apply a bio-optical algorithm to derive water quality parameters from the satellite-measured radiation.

The atmospheric correction includes three major processes that effects the ocean color sensing, notably: a) Rayleigh (molecule) scattering, b) absorption by water vapor, ozone and other gases, and c) absorption and scattering by suspended particles (aerosols). Whereas modeling of Rayleigh scattering and gas absorption is well established (Gordon *et al*., 1988) the main problem involves the correction from

suspended particles in the atmosphere because their size and distribution are highly variable in space and time (Gordon and Wang, 1994; Fraser *et al*., 1997; Tanre *et al*., 1997).

Historically, empirical models have been developed relating a radiative quantity (water-leaving radiance, upwelling radiance, volume reflectance or remote sensing reflectance) derived from color sensing instruments and chlorophyll concentration. For case I water, the basic chlorophyll algorithms are based on relationships between chlorophyll concentration and the ratio of reflectance (R) or water leaving radiance (Lw) at two wavelengths (443-490 and 550-580 nm). As mentioned before, these two bands describe the impact of absorption and scattering of light by chlorophyll pigment. The choice of a ratio approach, rather than another kind of combination lies in the variability and the uncertainty affecting the absolute value of R or Lw.

The retrieval of the chlorophyll content is thus performed by a four step processing chain:

(1) correction for the atmospheric contributions (Rayleigh scattering and gas absorption),

(2) estimation of the contribution of atmospheric aerosols using NIR data,

(3) derivation of a correction factor for aerosol scattering,

(4) retrieval of the water leaving radiance and application of the empirical band-ratio model.

Variations in the concentration of chlorophyll in the upper ocean and consequent changes in the penetration of visible light have a fundamental impact on prediction of biological, physical, and geo-chemical oceanographic processes. Phytoplankton absorbs solar energy and converts it to organic matter, thus providing the basis for the world fisheries production. Solar irradiance absorbed by the phytoplankton also contributes to changes in the underwater visibility as well as to variations in the local heating rate and thus influences the development of the thermal structure and dynamics of the upper ocean.

An example of global distribution of chlorophyll, respectively from March 1999 and February 2000 is shown in Figure 9. The deep blue and purple colors seen in most of the central ocean basins are oligotrophic waters resulting from selective absorption and scattering of pure seawater, unaltered from the presence of phytoplankton or other optically active substances. As one move closer to shore and shallow water regions nutrient inputs generally increase. The consequent development of higher concentrations of phytoplankton changes the color from blue to green.

Most of the empirical algorithms have been set up based on fitting ocean-color derived quantities to extensive world-wide in situ data set. However some algorithms have been developed for specific areas. Numerous empirical formulations have been proposed including Morel and Prieur (1977); Gordon *et al*., (1980); Gordon and Morel, (1983); Morel (1988) for CZCS algorithms, and O'Reilly *et al*., (1998) for SeaWiFS and OCTS algorithms.

In the open ocean the complexity of the ocean optics is not as severe as in the coastal areas (case II waters), where the sediments and colored dissolved organic matter (CDOM) also significantly contribute to the signal measured by the satellite sensors. Deriving water quality parameters, with a sufficient accuracy, in case II waters is one of the main challenge of the coming years in marine optics. The current development includes new sensors with improved capability, i.e., more and narrower spectral bands, and new algorithms with improved atmospheric correction scheme and/or global approach (inverse methods). The most advanced work is undertaken in connection with the development of the next generation of optical ocean color sensor, i.e., the US MODIS and the European MERIS instruments. The state-of-the-art in chlorophyll concentration retrieval in case II waters can be found in e.g., Doerffer and Fischer, 1994; Schiller and Doerffer, 1999; Moore *et al*., 1999, which discuss novel approaches such as inverse method, including artificial neural network techniques, and improved atmospheric correction algorithms.

Algorithm for estimating the primary production rate from satellite-derived chlorophyll and surface temperature was first proposed by Platt and Sathyendranath (1988). The state-of-the-art primary production models can be found in e.g. Antoine *et al*., 1996, and Behrenfeld and Falkowski, 1997. As phytoplankton absorb solar energy it removes inorganic carbon from the water, and reduce the partial pressure of carbon dioxide in the surface layers. In some cases, the partial pressure may be reduced below that in the overlying atmosphere resulting in a net flux of CO2 from the lower atmosphere to the upper ocean. Global estimation of primary production has therefore become one of the main applications of ocean color data because of its use as a proxy of the carbon cycle in the ocean (Figure 10).

The current challenge regarding ocean color remote sensing is to enable the combined and simultaneous use of all the sources of ocean color data in order to make a significant increase in coverage of the global ocean, which is of paramount importance in the context of the limitations of the sensors in the presence of clouds. This requires that the data from multiple sensors can be merged into a single global product, providing regular fields in space and time. This has not yet been accomplished with ocean-color data and is potentially a difficult task (Yoder *et al*., 1998).

NASA's Sensor Inter-comparison for Marine Biological and Interdisciplinary Ocean Studies (SIMBIOS) project aims at determining how data merging can be accomplished by defining standards for data level, quality definition, radiometric constraints, and algorithm implementation. Regarding the latter, the main expected improvements in light of the many new sensors are based on a systematic use of non-linear models, including cubic polynomial, power and hyperbolic-power relationships, as well as multiple regression approach.

4. OPERATIONAL OCEANOGRAPHY

Operational ocean forecasting systems relies on an integrated use of observations of physical, biological, and chemical variables and coupled physical and marine ecosystem models. These observations and the model dynamics are integrated using so called data assimilation techniques. These are mathematical techniques, which are usually based on some prior statistical assumptions about the accuracy of the observations and dynamical models. Essentially, these techniques provide a mean for introducing the information about the true ocean-state into the models, hence limiting the model drift away from the real state of the ocean.

The new operational data assimilation systems, which are being developed at several centers also demand observations which are available in near real time. Thus, an extensive effort must be invested in the development of real time data analysis and processing, as well as in data distribution.

The Global Ocean Data Assimilation Experiment (GODAE), for instance, aims to implement and operate (between 2003 and 2007) a global system of observations, communications, modeling and assimilation, that will deliver regular, comprehensive information on the 3D state of the global oceans. Its objectives are two-fold, notably: 1) Apply state-of-the art ocean models and assimilation methods for short-range open-ocean nowcasts and forecasts, and for boundary conditions to extend predictability of coastal and regional subsystems, and for initial conditions of climate forecast models; and 2) provide global ocean analyses for developing improved understanding of the oceans, improved assessments of the predictability of ocean systems, and as a basis for improving the design and effectiveness of the global ocean observing system.

At the onset of the new millennium we are therefore gradually transferring from satellite oceanography to operational oceanography. As indicated in Table 1 the suite of active microwave instruments currently in operation is providing for the first time consistent and regular global vector wind and wave fields, sea level and surface geostrophic height data in near real time (within three hours of observations), filling the gaps existing with conventional observation systems. This has opened up exiting new opportunities for wind, wave and current modeling, as well as assimilation into operational models for the production of marine weather, sea state and mesoscale current forecasts. Similarly, the large increase in the availability of optical sensors has lead to new opportunities for regular algae bloom monitoring which in turn has lead to pre-operational pilot demonstrations.

In this chapter we have selected to further address sea state, mesoscale current, sea ice and algae bloom in the context of operational oceanography.

4.1 Sea State

Satellite scatterometers provide a measure of both wind speed and direction over a swath of 500-1000 km width at a spatial resolution of 25-50 km. A complete global coverage is obtained in about three days. The quality of these wind field observations is widely recognized, and they enable for example small-scale low pressure systems and frontal lines to be identified properly compared with model background information. Provided the dual directional ambiguity of the vector wind field solutions are removed (Stoffelen and Andersen, 1997) the improvements in the initial wind field data provided by the scatterometer data have a beneficial impact on analyses and short-range forecasts, probably mainly from the improvements on the subsynoptic scales.

For example, the European Center for Medium-Range Weather Forecasting (ECMWF) provides operational meteorological forecast services, as well as sea-state forecasting services, to the national meteorological services of its seventeen participating states. The ERS scatterometer data are incorporated in such a way as to correct forecast surface wind fields continually over the oceans. These corrections are

then propagated through the numerical model to provide corrections to other parameters such as atmospheric pressure, temperature and humidity. Trials have demonstrated that the incorporation of scatterometer data improve the accuracy of the short-range forecasts by approximately five percent over forecasts where scatterometer data were not included. In particular, the use of scatterometer data to improve the accuracy of the wind data for tropical cyclones and hurricanes has proven very useful, so that initial values of atmospheric parameters at the model grid points better match the actual values. Since January 1996 the assimilation of ERS-2 scatterometer data has been fully operational at ECMWF.

In addition the availability of wave height data from the radar altimeter has provided a strong influence on wave modeling and has also stimulated the development of wave height assimilation techniques. One of the principal motivations for developing the third generation wave model WAM (Komen *et al.*, 1994) was to provide a state-of-the art model for the assimilation of global wind and wave data from satellites for improved wind and wave field analysis and forecasting. Presently, the WAM model is in use at a number of forecasting centers (NCEP, FNMOC, BMRC, and ECMWF to mention but a few) and altimeter wave height data are assimilated at MeteoFrance, KNMI, DNMI, UKMO and at ECMWF.

Moreover, as indicated in Table 1 the synthetic aperture radar (SAR) provides retrievals of the directional ocean wave spectrum either in wave mode operation (conducted in synergy with the scatterometer) or in full image mode. In the wave mode small SAR imagettes of 10 km x 5 km are acquired every 200 km along the scatterometer's near range coverage. These data are distributed to weather services for operational wave monitoring, analyses and forecasting (within three hours of observation) via the Global Telecommunication System (GTS). For the first time these data allow wave modelers to obtain global information on two-dimensional wave spectra.

In combination with the scatterometer wind field retrievals these data furthermore provide capabilities to separately study the wind sea, swell propagation and dissipation (Heimbach *et al*., 1998). This particularly has contributed to a provision of better open ocean wave forecasts since the ERS SAR wave mode data are allowing improved initialization of the swell field in the model. Moreover, the improved estimates of the wave spectrum (i.e. partitioning of the wave field into wind wave and swell components) are in turn used to refine wind field retrievals. Example of the direct application of such improved sea state prediction is associated with design of optimal ship routes.

In addition to the improvement in marine weather and sea state forecasting worldwide, the use of off-line products from ERS-1 is also providing benefits to the offshore industry as well as many other coastal activities. Time series of sea state information are being developed as a basis for predicting the sea state at a given time and location (Lasnier, 1996). This assists in a whole range of activities such as planning the timing and logistics of offshore activities to minimize risks to personnel, assessing marine risks, coastal defense planning, wave energy resource evaluations and setting engineering design parameters and is also helping insurance companies in risk analysis and the settlement of claims.

4.2 Mesoscale Ocean Current

Until 1996, operational ocean circulation models such as those run by the National Centres for Environmental Prediction (NCEP) and ECMWF (or several other numerical weather predictions centre) only assimilated sea surface temperature data from satellites. However, in recent years such models have began assimilating ERS-1/2 and T/P altimeter data on operational basis. The sea level heights from altimetry have been shown to increase the forecasting skill of the model, particular when salinity changes (in contrast to temperature) effect a large-scale change in sea level.

The need for a better monitoring and prediction of the marine environment has increased dramatically in recent years, in particular along the coastal boundaries and shelf regions where human activities are extensive and pollution has a significant impact. This has been documented in a number of

unpredicted events along coasts worldwide, such as storm surges, harmful algae blooms and oil spills. A common parameter of significant importance in this context is the surface current; known to satisfactory level of accuracy at high spatial and temporal resolution.

The oceanographic mesoscale is comprised of highly energetic features, including western boundary currents and their eddy fields as well as narrow coastal current systems. Routine monitoring of strong current features may provide extremely valuable information to for instance fishermen, pleasure sailors, merchant ship crews and oil platform operators.

Mesoscale monitoring has been successfully demonstrated with ERS and TOPEX/POSEIDON data in the Gulf of Mexico and Gulf Stream current system, and in the North Atlantic Azores front region. Since 1991, the Service Hydrographique et Océanographique de la Marine (SHOM) (French Navy) has been conducting a long-term program - called SOAP - aiming at developing operational oceanography for mesoscale applications taking advantage of the availability of TOPEX/POSEIDON and ERS-1 altimeter data. The system has documented to be extremely useful at providing monitoring and prediction of the Azores front and its associated mesoscale variability. Comparison with in-situ data gathered during the Semaphore experiment demonstrated the quality of the system. The follow on system, called SOPRANE, is implemented on a larger area (North-East Atlantic) and is currently assimilating TOPEX/POSEIDON and ERS-2 data.

Coastal models could also utilize altimetry to provide oceanic boundary conditions on the open ocean side of the model domain. Altimetry does not give highly accurate data near land, but the combination of suitable models incorporating the altimetry at their open boundaries would enhance coastal current forecasting.

The need for high quality predictions of marine parameters and processes has been well identified in EuroGOOS and there is currently an extensive activity in developing systems for operational monitoring and prediction of the marine environment. Examples are a number of EC funded projects which includes among others the Mediterranean Forecasting System Pilot Project (MFSPP), and the DIADEM and TOPAZ projects. The latter two include development and implementation of an operational assimilation system for physical and ecosystem variables for the North Atlantic, Nordic Seas and the Arctic Ocean. The DIADEM system, for instance, couples physical and biochemical model modules and assimilates satellite derived sea surface temperature, sea surface height and ocean color in a model covering the North Atlantic, Nordic Seas and Arctic Ocean.

4.3 Sea ice

The possibilities to measure ice drift from satellites has been radically improved over the last ten years. Over that period it has been used in several pilot demonstration projects, notably in Canada, the Baltic Sea and on the Siberian Coast, and is currently used operationally.

Largescale sea ice drift, which determines the advective part of the ice balance, can be derived from several types of low- and medium resolution satellite data: SSM/I, scatterometer and AVHRR data. Smaller scale ice motion including the formation of leads and polynyas, convergence with ridge formation and specific processes in the marginal ice zone such as eddies and ice tongues can only be measured by high-resolution Synthetic Aperture Radar (SAR) images, which have been available since the launch of ERS-1 in 1991 and further extended with RADARSAT in 1996.

The ice motion algorithm, also denoted ice motion tracker, is part of the RADARSAT Geophysical Processor System (RGPS) which is used routinely by Alaska SAR Facility to produce sea ice products from SAR images from the whole Arctic Ocean (Kwok, 1998).

The ice motion tracker is also used on SSM/I data to estimate large scale ice drift (Kwok *et al*., 1998) as shown in Figure 11. With the 85 GHZ channel it is possible to estimate ice motion every three days for the whole Arctic Ocean. Liu *et al* (1999) has demonstrated that also scatterometer data from NSCAT with 25 km resolution could be used successfully to calculate ice motion. Liu *et al*. (1999) has also shown that feature tracking using wavelet analysis can be a useful ice motion algorithm.

The presence of sea ice and its motion furthermore represents a major limitation for ships and offshore operations in at high latitudes in both hemispheres. The sea ice which is on average 2 - 3 m thick can only be penetrated by ice-strengthened vessels or icebreakers with sufficient ice class. Most ships and fishing vessels are not strengthened to sustain such conditions and must therefore avoid all ice areas. In many cases, when the ice concentration is 100 % and the ice pressure is high, even the most powerful icebreakers can have problems to move forward through the icepack. Offshore platforms operating in ice-covered areas must have much stronger construction than what is required in ice-free waters. Also harbours and loading terminals on the coast require stronger construction in areas of sea ice. In countries and regions were sea ice occur it is therefore of primary importance to monitor the sea ice regularly and produce ice forecasts to assist ship traffic, fisheries and other marine operations (Sandven *et al*., 1998). In the Northern Sea Route, the longest ice navigation route in the world, Russia has build up an extensive ice service to support the ship traffic (Johannessen *et al*., 1996). The service includes ice monitoring and forecasting as well as icebreaker escorting of cargo ships (Fig. 12).

The Canadian RADARSAT, operational from 1996, has sea ice monitoring as the prime objective and provides SAR data of ice covered areas on operational basis. With RADARSAT data, a new era in operational ice monitoring by satellites has begun, although there is still room for further research and development to advance ice scattering models and ice classification algorithms..

4.4 Algae Bloom

One of the main issues of surveying phytoplankton distribution and concentration is the operational monitoring of harmful algae blooms and potential fishery areas. The development of extreme algae bloom situations (harmful or not) generally depends on the following environmental conditions; (1) hydrodynamical conditions, (2) supply of macro-nutrients to the euphotic layer, (3) surface solar radiation, and (4) the optical properties of the water column. An algae bloom may have its peak activity below the surface, and hence may not be detected by remote sensors. The alga themselves have limited mobility and hence a measure of the advection of an identified bloom may be indirectly done through monitoring of the currents and ocean circulation pattern.

The goal of most harmful algae bloom (HAB) national plan is the effective management of fisheries, public health, and ecosystem problems related to marine biotoxins and harmful algae.

VNIR remote sensing data have already proved valuable for early warning of some algae blooms, and through use of information on front and gradients, a more efficient field sampling strategy can be implemented. In addition, routine monitoring data required for a forecast system provide a database containing information concerning the type, location, frequency, and duration of HABs. These data furthermore support studies on the impacts of HAB on the fisheries industry, on public health, and for basic algae and oceanographic research.

Figure 13 shows a SeaWiFS (left) and a NOAA-AVHRR (right) image from May 1999, covering the North Sea and Skagerrak area. The images resolve the pigment concentration in the water and the sea surface temperature, respectively. Major circulation and current patterns can be observed in both images. In particular the relatively cold and meso-trophic inflow of Atlantic water (in blue) in the Skagerrak is well observed, as well as the outflow of warm and eutrophic water from the Baltic.

In the same region, the outflow from the Oslofjord, characterized by high concentration of pigments, can be observed in the SeaWiFS image, as well as its spreading along the southeastern coast of Norway. High values are also observed, along the coast of Denmark. These originate from the high concentration of suspended matter, as well as the sea-floor contribution to the measured signal in this shallow water area. The mesoscale eddy variability along the western coast of Norway are also well captured in both images.

Despite the limitation in operational usage imposed by the presence of clouds, quality ocean color observation from space is valuable for early warning of algae bloom initiation and development in offshore areas. The derived products include chlorophyll a concentration, as an index of phytoplankton biomass, and the diffuse attenuation coefficient at 490 nm, as indicator of water clarity (Figure 14).

4.5 Emerging New Applications and Operational Services using imaging SAR

Whereas the quantitative retrievals of wind waves and swell from SAR are operational, regular services for oil spill detection and shallow water bathymetry monitoring are now also relying on SAR image data, although the methods are only possible in a certain range of wind field and sea state conditions. Recently, moreover, quantitative wind field retrievals from SAR data have improved significantly (EOQ, 1998; Beal and Pichel, 2000). On the other hand better quantitative interpretations must be developed for retrievals of mesoscale ocean features in order to improve the use of SAR observations in mesoscale ocean current monitoring and prediction system.

A brief overview of the current state-of-the-art SAR image retrievals of wind, oil spill and natural films, shallow-water bathymetry, and current features and internal waves, is provided below.

Wind: Quantitative information of the near surface wind field is derived from synthetic aperture radar (SAR) backscatter intensity measurements and their spectral properties. This allows higher spatial resolution regional and local wind fields at about 2 to 10 km to be derived (see Figure 15a, b). Such fields

are attractive for applications in coastal regions, smaller enclosed seas and in the vicinity of the marginal ice zones. This is not only for scientific interest (such as wind-wave coupling and air-sea interaction studies) but also for practical applications including towing operations, harbor and pilot boat operations, leisure boating and selection of sites for wind mills.

Following the launch of ENVISAT in 2001 data from a new and advanced synthetic aperture radar (ASAR) will become available. In addition to ensuring the continuity of the ERS SAR and RADARSAT observations (Figure 15 b) with a more versatile wave measurement mode, the ASAR instrument will offer new operating modes which look very promising for wind retrievals. In particular, the wide swath mode (150 m resolution) and global monitoring mode (1 km resolution) have the potential to deliver fine resolution wind field maps over a swath of more than 400 km.

This new and advanced capability to retrieve the fine resolution wind field from SAR clearly demonstrates the potential for new operational applications and research into coupled ocean-atmosphere interactive processes including atmospheric boundary and ocean mixed layer dynamics and exchanges of heat, momentum and gas across the ocean surface (Beal and Pichel, 2000).

Oil spills and natural films *:* Disaster management including flood (and sea level rise), toxic algae blooms and oil spill has been identified as a key area by the Committee on Earth Observation Satellites (CEOS) and Integrated Global Observing Strategy (IGOS). Extensive near real time use of SAR images for pollution monitoring along coastal waters are being conducted in several pre-operational projects (Pedersen *et al*., 1996).

It is clear that the imaging radars are very suitable for monitoring of oil spills notably in regions of intense ship traffic and in offshore areas of extensive oil and gas productions. Oil and natural slicks (film) dampens the capillary-short gravity waves on the ocean surface thus reducing or eliminating the

presence of Bragg scattering mechanism. In turn, the radar cross section is low and the imaged area appears dark.

Dependent on the characteristics of the observed pollutant features (and its source) there are various ways of responding to the near real time information provided by the imaging satellite radar such as redirection of patrol aircraft, request for information from nearby ships, and formal requests to refineries, industrial plants, rig operators or ships.

The basic question for most end users is distinguishing man-made oil spills from natural films and other "look-alike" features. For practical determination of slick type (whether natural or man-made) and origin using a single frequency and polarization SAR, empirical and conceptual and interactive algorithms, employing wind history and drift models, appear to be most useful (Espedal *et al*., 1998).

Shallow Water Bathymetry: Knowledge of sea bottom topographic features and corresponding depths is of vital importance to ship routing in shallow water, for fisheries and for offshore operations. While traditional bathymetric surveys are time and cost consuming, the imaging capabilities with SAR have demonstrated a promising capability to retrieve bathymetry maps over large areas at relatively low costs, provided the average water depth does not exceed 20 - 30 m.

Off the coast of the Netherlands it has been shown that large scale topographic structures, such as the Bruine Banken, are clearly imaged under favorable moderate (3-7 m/s) wind conditions. At low and high winds, on the other hand, the images can be dominated by the presence of natural films and speckle. The magnitude of the surface current further modulates the backscatter expressions. For example, in areas of strong current (order of 1 m/s), such as off the coast of Zeeland and in the Waddenzee, sand waves (typically of 2-6 m height and crest to crest separation of about 500 m) and other permanent topographic features are regularly observed in the SAR images.

SAR images are now used to retrieve bathymetry information and subsequently to validate and initiate morpho-dynamic models which are being developed to forecast changes in bottom shapes linked with sediment transport, river deposition and coastal erosion. The results of studies of bathymetry estimation in the Plaatgat area show that if the number of ship survey tracks is reduced by a factor of 3-5, the rms error of the assessed depth map is still less than 30 cm (Hesselman *et al*., 1997), which is the accuracy required by the Dutch Ministry of Transport and Public Works (Rijkswaterstaat). This conclusion is corroborated by the results of depth assessments in other areas. It demonstrates that the use of SAR remote sensing mapping techniques can lead to a substantial reduction of the costs of traditional sounding campaigns.

Current shear, convergence/divergence: An excellent documentation that the frontal features associated with the mesoscale circulation patterns are expressed in SAR images is shown in Figure 16 (Johannessen *et al*., 1996), where the surface roughness anomalies detected by the radar (right) are compared to the SST distribution imaged by the AVHRR (left). In the latter the structure of the SST field with the curvilinear temperature fronts represents mesoscale variability of 10 to 50 km scale, characteristic of the unstable Norwegian Coastal Current (Johannessen *et al*., 1989). The frontal features contained in the radar image have a configuration and orientation that are in good qualitative agreement with those in the AVHRR image.

In spite of such fascinating images, quantitative interpretation of these image expressions are still limited. In particular, simulations of such SAR backscatter signatures associated with current fronts and eddies appear less intense than the observed signatures in satellite SAR images. The magnitude of the predicted perturbation depends strongly on the angular dependence of both the short wave equilibrium spectrum and the relaxation rate on the wind direction. Since the parameterization of these are uncertain it is difficult to draw definitive conclusions regarding the quantitative accuracy of the models. To make

further progress at a fundamental level, it may be necessary to use more sophisticated wave generation and growth, nonlinear wave-wave interaction, wave-current interaction (including the effect of wave breaking), and radar backscattering models [18].

Internal waves : There are several types of internal wave (IW) signature expressions in the SAR images such as alternatively bright to dark, single dark and single bright bands of radar backscatter. The generation mechanisms of these are mostly explained by tidal current interaction with bathymetry in a stratified ocean. The anomalous expressions of the IWs are dependent on the existence of film material in the upper ocean as well as the strength of the near surface wind.

Simulation models give estimates of SAR backscatter signatures of IW patterns which are of the correct order of magnitude. For practical purposes, if internal waves are used to determine the hydrographic structure, it may be good enough just to determine the wave locations, wavelengths and propagation speeds from available SAR imagery. However, if we actually wish to estimate the strengths of the currents associated with the waves, it may be possible to apply an inversion scheme based upon one of these forward models (Brandt *et al*., 1999).

5. NEAR FUTURE SATELLITE OBSERVATION

The need to explore new Earth Observation capabilities aimed at bringing new data and scientific understanding has been elaborated in ESA's Earth Explorer Programme (ESA 98) and the US Earth Observing System (EOS) Science Plan (EOS 99). These program have been developed following extensive consultation with the Earth Observation communities, notably their concern about climate change and man's impact on it. Additional and complementary views and plans for Earth Observations regarding global climate change are implemented among other space agencies including CNES, NASDA, ISRO and Eumetsat. Views and plans are also naturally discussed by the Committee on Earth Observation Satellites [*i.e.* CEOS 97].

Furthermore as indicated in the listing of existing (and planned) operating satellite sensors according to the four classes identified in Table 1, notably, VNIR, TIR, PMW and AMW (Annex B) ensure that the number of continuity missions appear relatively secure for the next 5 to 10 years. In some instances, i.e. METOP, it is even guaranteed that scatterometry and VNIR/TIR operations will continue for 15 years.

Three geophysical quantities, that in different ways are relevant for important processes within the fields of cryosphere and oceanography, and which hitherto has not been observed from satellites are: a) the ice mass fluctuations; b) the sea surface salinity; and c) the marine geoid (and steady-state ocean circulation). It is generally agreed that the lack of these observations inhibits the development of scientific interpretation and understanding of basic processes that contribute to the ocean circulation and the effects of the ocean at seasonal to multi-decadal climate change as indicated in Table 3.

It is therefore comforting to know that the space agencies have approved missions concepts specifically focussed to observe these quantities. These mission plans include: ESA’s Cryosat mission

complemented by NASA's plans for the Ice, Clouds and Land Elevation Satellite (ICESat); ESA's GOCE mission and NASA's Gravity Recovery and Climate Experiment (GRACE) mission; and ESA's SMOS mission which to some extent is complemented by the ongoing joint NASA/NASDA Tropical Rainfall Measuring Mission (TRMM) and its planned follow-on mission. These missions are briefly discussed below.

Sea Ice Mass Fluctuations: The cryosphere has a central role in the Earth's radiation budget imposed by the large albedo due to the presence of ice and snow. Loss of sea ice is predicted to cause a larger greenhouse-gas warming in the Arctic than elsewhere on the Earth, whereas uncertainty in ice sheet and glacier mass balances are the largest error sources on present sea level change (Wingham, 98). Moreover, thermohaline circulation and deepwater formation are affected by changes in sea ice and ice sheet masses.

The primary goal of the Cryosat mission, planned for launch in 2002, is to estimate trends in the ice masses of the Earth. This will be achieved by measuring the change in sea ice and ice sheet thickness with a radar altimeter using interferometric and synthetic aperture techniques for resolution enhancement. Cryosat will provide nearly complete and continuous coverage of the cryosphere, but is limited in its resolution. The US ICESat mission planned for launch in 2001 is of particular complementary importance to Cryosat. ICESat aims to provide details of the sea ice and land ice roughness spectrum by employing a fine resolution (100 m scale) laser altimeter technique. The limits imposed by dense cloud cover will reduce sea ice thickness measurements and change measurements at fixed ice sheet locations. This will make optimal combination with the Cryosat radar altimeter very attractive.

Sea Surface Salinity: The distribution of salt in the global ocean and its annual as well as interannual variability are crucial in understanding the role of the ocean in the climate system. In-situ salinity measurements are only scarcely distributed over the oceans. In fact, 1˚ * 1˚ boxes distributed over

the global oceans show that for only about 70% of them a salinity measurements exists at all (Levitus and Boyer. 1994). A far smaller fraction of such areas has been monitored only once. This means that the average structures of the sea surface salinity (SSS) field are known to some extent, but details about its variability even on seasonal and interannual scales remain hidden.

The SSS varies as a result of exchange of water between the ocean and the atmosphere, via sea ice freezing and melting and from continental runoff. Salt affects the thermohaline circulation and therefore the distribution of mass and heat. Salinity may control the formation of water masses, which allows its use for tracer studies. Salinity is also thermodynamically important as salinity stratification can influence the penetration depth of convection at high latitudes and may determine the mixed layer depth in equatorial regions through the evaporation-precipitation coupling.

The sensitivity of L-band (1.4 GHz) passive microwave radiometer measurements of oceanic brightness temperature to SSS is well established (Lagerloef *et al*., 1995, Kerr *et al*., 1999). However, the sensitivity is a function of the sea surface temperature (SST) decreasing from 0.5 K/psu in 20˚ C water to 0.25 K/psu for an SST of 0˚ C. Hence, strong demands are put on the SSS retrievals from space in polar and sub-polar regions where the water masses are very sensitive to small changes in SSS (below 0.1 psu). Other oceanic factors which will influence the brightness temperature retrievals at L-band are surface roughness (wind speed and direction) and foam. Precise estimates for the uncertainties associated with these features are required in order to obtain sufficiently accurate SSS retrievals from space.

The ESA SMOS mission duration is planned for three years in order to cover two complete seasonal cycles, with a candidate launch date in 2005. Complementarity and synergy with other operating passive and active microwave system are foreseen and in particular it will provide extremely valuable data for constraining the evaporation minus precipitation budget over the tropical oceans provided a TRMM follow-on mission is flown simultaneously.

Marine Geoid and Steady-State Ocean Circulation: While variations of the sea level and thus of the ocean currents can be derived directly from satellite altimeter data, the absolute value of the ocean dynamic topography, and hence the absolute surface circulation, requires the independent determination of what would be the elevation of an ocean at rest, that is the geoid. The latter is not known at present with sufficient precision. The typical elevation scale of the dynamic topography is of the order of 0.1 to 1 m, while the precision of present geoid models is also multi-decimetric on the scale of many ocean circulation features.

The scientific objectives of the GOCE Mission are, based on the unique measurements by the gravity gradiometer and satellite-to-satellite tracking in high-low mode, to provide an accurate and detailed global model of the Earth's gravity field and geoid (ESA-99) with an accuracy of 1mgal and 1 cm at a spatial resolution of 100 km.

GOCE is complementary with GRACE . GRACE will be the first gravity field mission using the principal of satellite-to-satellite low-low tracking mode. It will improve the accuracy of the spherical harmonic coefficients at the long and medium spatial scales (< ~ 500 km) by up to three orders of magnitude. This will allow measurement of the temporal variations in the gravity field to be recovered at 30-90 days interval over a period of about 5 years (planned to begin in 2001). Over the ocean this means that bottom pressure variations can be derived at a typical horizontal scale of 1000 km whereas changes in the ice masses can be studied over Antarctica and Greenland Ice Sheets. The aim (and challenge) is then to convert these sea floor pressure variations to changes in global ocean circulation.

6. SUMMARY

No in-situ observing system is presently conceivable on global scale, except perhaps underwater acoustic tomography. On the other hand no satellite remote sensing system provide sufficient subsurface observations. It is therefore only via the systematic combination of both observing systems that a 3 D picture of the oceanic state can be drawn. Moreover, only with models able to assimilate data and simulate the 3 D oceanic state can we conclude that we have a fully integrated system that can provide realistic forecasts.

Over the past two decades, the tools to observe, understand and model the Earth system have improved substantially through developments in observational technology, including remote sensing from space, through improvements in numerical simulation and high performance computing, and through new methods for assimilation of the time dependent atmospheric, oceanic and chemical data in an hierarchical set of dynamically evolving models. This has deepened our understanding of the complex interactions between the various components of the Earth system which together govern the evolution of the system as schematically illustrated in Figure 17.

In this perspective, satellites offer unique capabilities as they provide global, quasi-synoptic and repetitive data sets of homogeneous quality. The number of geophysical and bio-chemical variables that can be measured from space is large as indicated in Table 1, and addresses most components of the Earth System. All these characteristics of remote sensing from space are essential as the system itself is continuously changing over a wide range of space and time scales. Space observations have a key role to play in research and monitoring of the Earth system as they often provide the only means to require the relevant data.

However, it must be emphasized that the overall long term design criteria of the ocean observing system for climate, expressed by the Oceans Observation System Development Panel (OOSDP), is:

> 'to monitor, describe and understand the physical and biogeochemical processes that determine ocean circulation and the effects of the ocean on seasonal to decadal climate change, and to provide the observations necessary for climate predictions'

During the first decade of the new millennium relatively long time series (in some cases almost 30 years) of satellite derived quantities (including sea surface temperature, ocean wave field, near surface wind, ocean color, sea surface topography and sea ice extent, types and concentration) will become available. As an essential element of integrated ocean observing systems (in combination with in situ data collection system and model tools) continuous access to calibrated and corrected satellite data is indisputable. No space agency by itself can ensure to meet such a continuity requirement. International cooperation in implementation and operation of key missions is therefore highly necessary. This will also avoid duplication and ensure complementarity, and should lead to significant reductions in the each agencies costs of addressing the objectives of the ocean observing system for climate. The challenge is furthermore, to ensure the continuity of existing Earth observation data while at the same time developing new observation techniques. In the first decade of the new millennium Earth Observation from satellites, as an integrated part of the Global Ocean Observing System for Climate (http://www-ocean.tamu.edu/OOSDP/FinalRept) will be faced with exactly this challenging requirement.

Future plans and implementation of new Earth Observation satellite missions must also maintain a degree of flexibility to ensure optimum adjustment and complementarity with development and improvements of models and their subsequent need for data. The same is valid vis-à-vis technology development for in situ instruments. Regarding the latter, rapid development is undergoing for smart, autonomous expendable system and unmanned observing vehicles that return data via telemetry. The

deployment of up to 3000 profiling Argo floats is one such example of a new and powerful element of a comprehensive international system for observing the global ocean. The expectation regarding future implementation of acoustic tomography and thermometry are other examples.

Acknowledgement

We are grateful to colleagues at the Nansen Environmental and Remote Sensing Center and at universities, research institutes and centers elsewhere for their valuable comments and support in making this article. Especially our thanks go to Ola M. Johannessen, Lasse Pettersson, Martin Miles, Elena Shalina, Einar Bjørgo, Pierre-Yves Le Traon, Paris W. Vachon, Steve Groom, and Marcos Portabella. We are also grateful to have received permissions to reproduce figure materials in this book-article. This is further specified in the figure captions. Financial support for this work has been obtained from Norwegian Space Centre, European Space Agency and Norwegian Research Council.

7. REFERENCES

Antoine, D., J.-M. André, and A. Morel, 1996. Oceanic primary production 1. Adaptation of a spectral light-photosynthesis model in view of application to satellite chlorophyll observations, *Global Biogeochem. Cycles*, 10, 43-55,

Beal, R.C. and W.G. Pichel, 2000, Coastal and Marine Applications of Wide Swath SAR, Johns Hopkins APL, *Technical Digest,* vol. 21, No. 1

Behrenfeld, M. J., and P. G. Falkowski, 1997. Photosynthetic rates derived from satellite-based chlorophyll concentrations, *Limnol. Oceanogr.*, 42, 1-20.

Bijlsma, L. (and 18 co-authors), 1996, Impacts, adaptions and mitigation of climate chang: scientific-technical analysis, Contribution to 2nd Assessment Report of the Intergovernmental Panel on Climate Change, eds. J.T. Houghton, *et al*., *University Press,* 572 pp.

Bjørgo, E., O. M. Johannessen and M. W. Miles, 1997 Analysis of merged SMMR/SSMI time series of Arctic and Antarctic sea ice parameters. *Geophys. Res. Lett.* 24, 413 – 416.

Brandt, P., R. Romeiser, and A. Rubino, 1999, On the determination of characteristics of the interior ocean dynamics from radar signatures of internal solitary waves, *Journal of Geophys. Res.,* 104, 30039-30047.

Campbell, W. J. NASA remote sensing of sea ice AIDJEX, Proceedings of the World Meteorological Organization Technical Conference, Tokyo, Japan, WMO No. 350, pp. 55 -56, 1973.

Carsey, F., 1992, *Microwave Remote Sensing of Sea Ice,* Geophysical Monograph 68, American Geophysical Union., p. 462.

Cavalieri, D., P. Gloersen, W.J. Campbell, 1984, Determination of sea ice parameters with the Nimbus 7 SMMR, *Journal of Geophys. Res*., 89 (D4), 5355-5369.

Cavalieri, D.J., P. Gloersen, C.E. Parkinson, H.J. Zwally and J.C. Comiso, 1997: Observed hemispheric asymmetry in global sea ice changes. *Science,* 278, 1104-1106.

CEOS 97: Committee on Earth Observation Satellites: Toward and Integrated Global Observing Strategy, 1997 CEOS Yearbook, Published by Smith System Engineering Limited, UK.

Coles, S.G. and J.A. Tawb, 1990, *Statistics of coastal flood prevention, Philosophical Transactions of the Royal Society of London*, A332, pp. 457-476.

Comiso, J.C.,1986, Characteristics of Arctic winter sea ice from satellite multispectral microwave observations, *Journal of Geophys. Res*., 91(C1), 975-994.

Denman, K., E. Hofmann and H. Marchant, 1996. Marine biotic responses to environmental change and feedbacks to climate. In Climate change 1995, J.T. Houghton, L.G. Meira, B.A. Callander, N. Harris, A. Kattenberg and K. Maskell eds., IPCC, pp. 487-516.

Doerffer R. and J. Fischer, 1994. Concentration of chlorophyll, suspended matter, and glebstoff in case II waters derived from satellite coastal zone color scanner data with inverse modeling methods. *J. Geophys. Res*., 99(C4): 7457 – 7466.

Elachi, C. 1987, *Spaceborne Remote Sensing: Applications and Techniques*, IEEE Press.

Emery W.J., G. A. Wick and P. Schluessel, 1995, Skin and Bulk Sea Surface Temperatures: satellite Measurement and Corrections, *Oceanographic Applications of Remote Sensing,* (editors: M. Ikeda and F.W. Dobson) CRC Press, pp.145-164.

EOS. The US EOS Science Plan: The State of Science in the EOS Program, NASA NP-1998-12-069-GSFC, January 1999.

EOQ, *Earth Observation Quarterly*, No. 59, July 1998, ESA publication division, Noordwijk, The Netherlands.

ESA SP-1227, 1998, The Science and Research Elements of ESA's Living Planet Program, *ESA Publication Division, SP-1227,* Noordwijk, The Netherlands.

ESA SP-1233, 1999, Report for Mission Selection, Gravity Field and Steady-State Ocean Circulation Mission, *ESA Publication Division, SP-1233*, Noordwijk, The Netherlands.

Espedal, H.A., O.M.Johannessen, J.A.Johannessen, E. Dano, D. Lyzenga and J.C.Knulst, COASTWATCH'95, A tandem ERS-1/2 SAR detection experiment of natural film on the ocean surface, *Journal of Geophysical Research-Ocean,* vol. 103, Oct.15, pp. 24969-24982.

Fraser, R.S., S. Matto, Yeh Eueng-Nan, C.R. McClain, 1997. Algorithm for atmospheric corrections of satellite measurements of ocean pigment. *J. Geophys. Res*., 102(D14), 17,107 – 17, 118.

Gaspar,P. and J.P.Florens, 1998, Estimation of the sea state bias in radar altimeter measurements of sea level: Results froma new non-parametric method, *Journal of Geophys. Res.,* 103(C8), 15803-15814.

Gloersen, P., W. J. Campbell, D. J. Cavalieri, J. C. Comiso, C. L. Parkinson and H. J. Zwally. *Arctic and Antarctic Sea Ice, 1978 - 1987. Satellite Passive-Microwave Observations and Analysis*. NASA SP-511, 1992, 290 pp.

Gohin, F. and A. Cavanie, 1994, A first try at identification of sea ice using the three beam scatterometer of ERS-1, *Int. Journal of Remote Sensing,* 15(6), 1221-1228.

Gordon H.R., 1997. Atmospheric correction of ocean color imagery in the Earth Observing System era. *J. Geophys. Res*., 102(D14), 17,081-17,106.

Gordon, H.R., D.K. Clark, J.L. Mueller, W.A. Hovis, 1980. Phytoplankton pigments derived from the Nimbus-7 CZCS: initial comparisons with surface measurements. *Science*, 210, 63-66.

Gordon H. R., A. Morel, 1983. Remote assessment of ocean color for interpretation of satellite visible imagery, a review. Lecture notes on coastal and estuarine studies. Springer-Verlag , 114 p.

Gordon, H.R., J.W. Brown, R. Evans, 1988. Exact Rayleigh scattering calculations for use with the Nimbus--7 Coastal Zone Color Scanner. *Appl. Opt.*, 27: 862-871.

Gordon, H.R., .M. Wang, 1994. Retrieval of water-leaving radiance and aerosol optical thickness over oceans with SeaWiFS: a preliminary algorithm. *Appl. Opt.,* 33(3): 443--452.

Grandell, J., J.A.Johannessen, and M. Hallikainen, 1999, Development of a synergetic sea ice retrieval method for the ERS-1 AMI wind scatterometer and SSM/I radiometer, *IEEE Trans. Geoscience Remote Sens.*, 37(2), 668-679.

Halpern, D. (ed), 2000. Satellites, Oceanography and Society, Elsevier Oceanographic Series, 63, Amsterdam, The Netherlands.

Heimbach, P., S. Hasselmann, and K. Hasselmann, Statistical analysis and interpretation of WAM model data with global ERS-1 SAR wave mode spectral retrievals over 3 years, vol 103, no. C4, pp. 7931-7979, April 15, 1998, Advances in Oceanography and Sea Ice Research using ERS Observations, *Journal of Geophysical Research-Ocean*.

Hesselmans, G. C. Calkoen and H. Wensink, Mapping of Seabed topography to and from SAR, ESA SP-414, May 1997, In Proceedings Third ERS Symposium, Space at the service of our Environment, ESA Publication Division.

Johannessen, O. M., W . J. Campbell, R. Shuchman, S. Sandven, P. Gloersen, J. A. Johannessen, E. G. Josberger and P. M. Haugan, 1992. Microwave study programs of air-ice-ocean interactive processes in the seasonal ice zone of the Greenland and Barents seas. Chapter 13 in *Microwave Remote Sensing of Sea Ice* (Editor F. Carsey) AGU Geophysical Monograph 68, pp. 261 - 289.

Johannessen, O. M., A. M. Volkov, V. D. Grischenko, L. P. Bobylev, S. Sandven, K. Kloster, T. Hamre, V. Asmus, V. G. Smirnov, V. V. Melentyev and L. Zaitsev, 1997. ICEWATCH - Ice SAR monitoring of the Northern Sea Route. In "*Operational Oceanography. The Challenge for European Co-operation*" (Editor in Chief: J. H. Stel). Proceeedings of the First International Conference on

EuroGOOS, 7 -11 October 1996, The Hague, The Netherlands. Elsevier Oceanography Series, No. 62, pp. 224 - 233.

Johannessen, O.M., M. Miles and E. Bjørgo, 1995: The Arctic's shrinking sea ice. *Nature,* 376, 126-127.

Johannessen, O.M., E.V. Shalina and M.W. Miles, 1999, Satellite Evidence for an Arctic Sea Ice Cover in Transformation, *Science*, 286, 1937-1939.

Johannessen, J.A., E. Svendsen, S. Sandven, O.M. Johannessen and K. Lygre, 1989, Three Dimensional Structure of Mesoscale Eddies in the Norwegian Coastal Current, *Journal of Phys. Oceanography,* 19(1), 3-19.

Johannessen, J.A., R.A. Shuchman, G. Digranes, D. Lyzenga, Wkerman, O.M.Johannessen and P.W.Vachon, 1996. Coastal ocean fronts and eddies imaged with ERS-1 SAR, *Journal of Geophys. Res.,* 101(C3), 6651-6668.

Kerr, Y. *et al*., SMOS: Soil Moisture and Ocean Salinity, Proposal selected under the ESA Living Planet Program: Earth Explorer Opportunity Mission, April, 1999.

Komen, G.J., L. Cavaleri, M. Donelan, K. Hasselmann, S. Hasselmann and P.A.E.M. Janssen, 1994, Dynamics and Modelling of Ocean Waves, *Cambridge University Press*, 532 pp.

Kwok, R., 1998, The RADARSAT Geophysical Processor System, In Analysis of SAR data of the Polar Oceans: Recent Advances, eds.: C. Tsatoulis and R. Kwok, *Springer Verlag*. pp. 235-257.

Lagerloef, G.S.E., C.T. Swift, D.M. Le Vine, 1995, Sea surface salinity: Th next remote sensing challenge, *Oceanography,* 8, 44-50.

Lasnier, P., February, 1996, *In ESA SP-1176/II, New Views of the Earth: Application Achievements of ERS-1*, ESA publication division, Noordwijk, The Netherlands.

Le Traon, P.-Y. and F. Oger, 1998, ERS-1/2 orbit improvement using the TOPEX/POSEIDON: The 2 cm challenge, Advances in Oceanography and Sea Ice Research using ERS Observations, *J. Geophys. Res.*, 103(C4), 8045-8058.

Le Traon, P.Y. and G. Dibarboure, 1999. Mesoscale mapping capabilities from multiple altimeter missions. *J. Atmospheric Oceanic Technology.*, 16, 1208-1223

Liu, A.K., Y. Zhao, and S.Y. Wu, 1999, Arctic sea ice drift from wavelet analysis of NSCAT and SSM/I data, *J. Geophys. Res.*, 104(C5) , 11,529-11,538.

Levitus, S., T.P. Boyer, 1994, World Ocean Atlas 1994, Volume 4: Temperature, NOAA Atlas NESDIS 4, NOAA, 117 pp.

McClain E.P., W.G. Pichel, C.C. Walton, 1985. Comparative performance of AVHRR-based multichannel sea surface temperatures. *J. Geophys. Res.*, 90(C6), 11587–11601.

Meier, M.F., 1984, Contribution of small glaciers to global sea level, *Nature*, 343, 115-116.

Moore, G.F., J. Aiken and S.J. Lavender, 1999. The atmospheric correction of water colour and the quantitative retrieval of suspended particulate matter in Case II waters: application to MERIS. *Int. J. Remote Sensing*, 20, 1713-1733.

Morel, A. and L. Prieur, 1977. Analysis and variations in ocean color. *Limnol. Oceanogr.*, 22(4):709-722.

Morel, A., 1988. Optical modeling of the upper ocean in relation to its biogenous matter content (case I waters*). J. Geophys. Res.*, 93(C9), 10,749 – 10,768.

Morel, A., 1998. Minimum requirements for an operational ocean-color sensor for the open ocean. Report of the IOCCG No. 1, Ed. IOCCG. Darthmouth, Canada, 46 p, ISSN 1098-6030.

O'Reilly J.E., *et al.* 1998. Ocean color chlorophyll algorithms for SeaWiFS. *J. Geophys. Res.,* 103(C11), 24,937–24,953.

Pedersen, J.P. *et al.*," Oil spill detection by use of ERS SAR data - From R&D towards pre-operational early warning detection service" February, 1996, ESA SP-383, *Proceedings Second International Workshop on ERS Applications*, ESA publication, division, Noordwijk, The Netherlands.

Piexoto, J.P. and A.H. Oort, The Physics of Climate, American Institute of Physics, New York, 1992.

Platt, T. and S. Sathyendranath, 1988. Oceanic primary production: estimation by remote sensing at local and regional scales. *Sciences*, 241, 1613–1620.

Robinson, I.S., 1985. Satellite oceanograhy: an introduction for oceanographers and remote-sensing scientists. John Wiley & sons eds., 455 p.

Sandven, S. O. M. Johannessen, M. W. Miles, L. H. Pettersson and K. Kloster, 1999. Barents Sea seasonal ice zone features and processes from ERS-1 SAR: SIZEX92 . *J. Geophys. Res*., 104(C7), 15,843-15,858.

Sandven, S., H. Gronvall, A. Seina, H. H. Valeur, M. Nizovsky, H. Steen Andersen and V. E. J. Haugen. Operational Sea Ice Moniotring by Satellites in Europe. OSIMS Final report. NERSC Technical Report no. 148, June 1998, 91 pp.

Schiller, H.and R. Doerffer, 1999, Neural network for emulation of an inverse derivation of case II water properties from MERIS data, *Int. J. Remote Sens.,* 20(9), 1735-1746.

Smith, D. M., 1998, Recent increase in the length of the melt season of perennial Arctic sea ice. *Geophys. Res. Lett*., 25, 655-658.

Smith, N. and C. Koblinsky (eds), 2001. Observing the Ocean for Climate in the 21st Century, Bureau of Meteorology, Melbourne, Australia.

Steffen, K., J. Key, D. J. Cavalieri, J. Comiso, P. Gloersen, K. St. Germain and I. Rubinstein, 1992,. The Estimation of Geophysical Parameters using Passive Microwave Algorithms. Chapter 10 in *Microwave Remote Sensing of Sea Ice* (Editor F. Carsey) AGU Geophysical Monograph 68, pp. 201 – 231.

Stoffelen, A. and D. Andersen, Ambiguity removal and assimilation of scatterometer data, pp. 491-518, 1997, *Q.J.R. Meteorol. Soc*. 123.

Stogryn, A., 1971, Equations for calculating dielectric constant of saline water. *IEEE Trans. Microwave Theory Tech*., MTT-19, 733-736.

Svendsen, E.A., K.Kloster, B.A. Farrelly, O.M.Johannesen, J.A.Johannessen, W.J. Campbell, P.Gloersen, D. Cavalieri and C. Matzler, 1983, Norwegian Remote Sensing Experiment: Evaluation of the Nimbus 7 Scanning Multichannel Microwave Radiometer for Sea Ice Research. *J. Geophys. Res.*, 88(C5), 2781-2791.

Svendsen, E., C. Mätzler, and T.C. Grenfell, 1987, A model for retrieving total sea ice concentration from spaceborne dual-polarized passive microwave instrument operating near 90 GHz, *Int. J. Remote Sens.,* 8(10), 1479-1487.

Tanré D., Y.J. Kaufman, M. Herman, S. Mattoo, 1997. Remote sensing of aerosol properties over oceans using the MODIS/EOS spectral radiances. *J. Geophys. Res.*, 102(D14), 16,971-16,988.

Yoder, J.A., *et al.*, 1998. Status for satellite ocean-color missions: considerations for complementary missions. Report of the IOCCG No. 2, Ed. IOCCG. Darthmouth, Canada, 46 p, ISSN 1098-6030

Ulaby, F. T., R. K. Moore and A. K. Fung. 1982, Real Aperture Side-Looking Airborne Radars, in *Microwave Remote Sensing - Active and Passive*: Volume II - Radar Remote Sensing and Surface Scattering and Emission Theory, Addison-Wesley Publishing Co., Reading, MA, pp. 562 – 629.

Ulaby, F. T., R. K. Moore and A. K. Fung, 1982, Synthetic Aperture Side-Looking Airborne Radar Systems, in *Microwave Remote Sensing - Active and Passive*: Volume II - Radar Remote Sensing and Surface Scattering and Emission Theory, Addison-Wesley Publishing Co., Reading, MA, pp. 630 - 745.

Vachon, P.W., P. Adlakha, H. Edel, M. Henschel, B. Ramsey, D. Flett, M. Rey, G. Staples and S. Thomas, 2000, Canadian Progress Towards Marine and Coastal Applications of Synthetic Aperture Radar, Johns Hopkins APL, *Technical Digest,* 21(1), 33-40.

Warrick, R.A., C. Le Provost, M.F. Meier, J. Oerlemans, P.L. Woodworth, 1996, The science and climate change, Contribution to 2nd Assessment Report of the Intergovernmental Panel on Climate Change, eds. J.T. Houghton, *et al.*, *University Press,* 572 pp.

Wingham, D. *et al.*, 1999, CRYOSAT, A mission to determine fluctuations in the mass of the Earth's land and marine ice fields, Proposal selected under the ESA Living Planet Program: Earth Explorer Opportunity Mission, April.

Wright, J.W., 1978, Detection of ocean waves by microwave radar: The modulation of short gravity-capillary waves, *Boundary Layer Meteorol.,* 13, 87-105.

Wentz, F.J., C. Gentemann, D. Smith and D. Chelton, 2000, Satellite Measurements of Sea Surface Temperature through clouds, *Science,* 288, 847-850.

ANNEX A. ABBREVIATIONS AND ACRONYMS

AMW	Active Microwave
ASAR	Advanced Synthetic Aperture Radar
AVHRR	Advanced Very High Resolution Radiometer
CEOS	Committee on Earth Observation Satellites
CZCS	Coastal Zone Color Scanner
DMSP	Defense Meteorological Satellite Program
EC	European Commission
ECMWF	European Center for Medium-Range Weather Forecasting
EM	Electromagnetic
ENVISAT	Environmental Satellite
EO	Earth Observation (normally meaning the use of space-borne data)
ERS	European Remote Sensing Satellite
ERTS	Earth Resource Technology Satellite
ESA	European Space Agency
EuroGOOS	European Association for the Global Ocean Observing System
FCCC	UN Framework Convention on Climate Change
FY	Firstyear
GLI	Global Imager
GOCE	Gravity Field and Steady-state Ocean Circulation Explorer
GODAE	Global Ocean Data Assimilation Experiment
GOOS	Global Ocean Observing System
GPS	Global Positioning System
GRACE	Gravity Recovery and Climate Experiment
IGBP	International Geosphere and Biosphere Program
IOC	Intergovernmental Oceanographic Committee
IPCC	Intergovernmental Panel on Climate Change
IR	Infra-Red
LRI	Low Resolution Image
MERIS	Medium Resolution Imaging Spectroradiometer
METOP	Meteorological Operational
MISR	Multi-angle Imaging Spectroradiometer
MODIS	Moderate Resolution Imaging Spectroradiometer
MOS	Modular Opto-electronic Scanner
MY	Multi-year
NESDIS	National Environmental Satellite, Data & Information Service
NOAA	National Oceanic and Atmospheric Administration, USA
NORSEX	Norwegian Remote Sensing Experiment
NSCAT	NASA Scatterometer
OCI	Ocean Color Imager
OCM	Ocean Colour Monitor
OCTS	Ocean Color and Temperature Sensor
OOSDP	Ocean Observation System Development Panel
OSMI	Ocean Scanning Multispectral Imager
PMW	Passive Microwave

POLDER	Polarisation and directional
SAR	Synthetic Aperture Radar
SeaWiFS	Sea Wide Field of view Sensor
SIMBIOS	Sensor Inter-comparison for Marine Biological and Interdisciplinary Ocean Studies
SIZEX	Seasonal Ice Zone Experiment
SLR	Side-Looking Radar
SMMR	Scanning Multi-channel Microwave Radiometer
SMOS	
SSM/I	Special Sensor Microwave Imager
SSS	Sea Surface Salinity
SST	Sea Surface Temperature
TIR	Thermal Infrared
TMI	TRMM Microwave Imager
TRMM	Tropical Rainfall Microwave Measurements
VNIR	Visual and Near-Infrared
WAM	Wave Model
WCRP	World Climate Research Program
WMO	Word Meteorological Organization
WWW	World Weather Watch

ANNEX B. LIST OF SELECTED EO SATELLITES AND SENSORS FOR OCEANOGRAPHY: PAST, PRESENT, FUTURE

A list of the most common Earth observation satellites (past, present and future) and sensors is provided in this annex, together with some relevant sensor and satellite characteristics:

- Under the **satellite** column the name of the spaceborne platform is provided.
- In the **Instrument** column we make reference to the type of technology used and/or measurements performed by a given sensor.
- Under **acronym**, we give the common name used for a given sensor.
- The **swath width** is the size of the across track area on the ground which is covered by the instruments.
- The **spatial resolution** is approximately the size of the smallest feature on the ground that can be resolved with the instrument.
- The availability of data is given in terms of the **operating period** for past sensors, the start of the operating period for present sensors, and the approved/planned launch-date for future satellites.

Past

Satellite	Instrument	Acronym	Swath width	Spatial Resolution	Operating period
VNIR only					
ADEOS-1	Polarization and Directionality of the Earth's Reflectance	POLDER	1400 km	7x6 km	1996-1997
VNIR and TIR					
Nimbus-7	Coastal Zone Ocean Scanner	CZCS	1600 km	0.825 km	1978-1986
ADEOS-1	Ocean Color and Thermal Scanner	OCTS	1400 km	0.700 km	1996-1997
NOAA-1-8	Advanced very high resolution radiometer	AVHRR/1	3000 km	1.1 km	1972 – 1984
ERS 1	Along-Track Scanning Radiometer	ATSR (TIR only)	500 km	1 km	1991-1996
PWM					
SeaSat	Scanning Multichannel Microwave Radiometer	SMMR	3000 km	Function of the frequency (30 - 150 km)	1978
Nimbus-7	Scanning Multichannel Microwave Radiometer	SMMR	3000 km	Function of the frequency (30 - 150 km)	1978-1988
AMW					
SeaSat	Synthetic Aperture Radar	SAR	100 km	25m	1978
	Wind-Scatterometer	SASS	750 km	50 km	
	Altimeter	RA		5 - 30 km	
ERS-1	Synthetic Aperture Radar	SAR	100 km	30 m	1991-1996
	Wind Scatterometer	AMI-WIND	500 km	50 km	
	Altimeter	RA		7 km	
JERS-1	Synthetic Aperture Radar	SAR	75 km	18 m	1992 – 1995
ALMAZ-1	Synthetic Aperture Radar	SAR	40–350 km	10 - 15 m	1991 – 1992
ADEOS-1	Scatterometer	NSCAT	600 km	50 km	1996-1997
GEOSAT	Altimeter	GEOSAT	NA	6.7 km	1985-1990

NA: not applicable

Present

Satellite	Instrument	Acronym	Swath width	Spatial Resolution	Operating period
VNIR only					
Orbview-2	Sea-viewing, Wide Field Sensor	SeaWiFS	1500-2800 km	1.1km / 4.4km	From 1997-
Oceansat-I	Ocean Colour Monitor	OCM	1500 km	350 m	From 1999
EOS-AM1	Multi-angle Imaging Spectroradiometer	MISR	370 km	275 m	From 1999
Kompsat	Ocean Scanning Multispectral Imager	OSMI	800 km	850 m	1999
VNIR and TIR					
LANDSAT 5 LANDSAT-7	Thematic Mapper Enhanced TM	TM ETM+	185 km 705 km	120m (TIR) 60m (TIR)	From 1976 From 1999
NOAA-POES NOAA-9-14; K-N	Advanced very high resolution radiometer	AVHRR/2 AVHRR/3	approx. 3000 km	1.1 km	From 1984
ERS 2	Along Track Scanning Radiometer	ATSR (TIR only)	500 km	1 km	From 1995
PRIRODA (MIR)	Modular opto-electronic scanner	MOS	82 km	650 m	1995 – 1999
IRS-P3	Modular opto-electronic scanner	MOS	200 km	520	From 1996
ROCSAT-1	Ocean color imager	OCI	690 km	0.825 km	From 1999
EOS-AM1	Moderate Resolution Imaging Spectro Radiometer	MODIS	2300 km	250m / 1000m	From 1999
EOS-AM1	Advanced Spaceborne Thermal Emission and Reflection Radiometer	ASTER	60 km	90m (TIR)	From 1999-
NOAA-GOES 8-10	Visible and IR Spin Scanning Radiometer	VISSR	Horizon to horizon	1km (VNIR.) 7 & 14km (TIR)	From 1975
GMS Program GMS-5	Visible and IR Spin-Scan Radiometer	VISSR	Full Earth disk*	1.25km (VNIR) 5km (TIR)	From1984
Meteosat program Meteosat-7	Visible and IR Spin-Scan Radiometer	MSR	Full Earth disk*	2.5 km (VNIR) 5 km (TIR)	From 1989

*: Swath width for geostationary satellite are indicated as full Earth disc.

Present (cont.)

Satellite	Instrument	Acronym	Swath width	Spatial Resolution	Operating period
PWM					
DMSP	Microwave Imager	SSM/I	1400 km	25 - 50 km	From 1987
TRMM	Microwave imager	TMI	760 km	4.4 – 45 km	From 1997
Oceansat-I	Microwave imager	MSMR	1360 km	40 to 120 km	From 1999
AMW					
ERS-2	Synthetic Aperture Radar Wind Scatterometer Altimeter	SAR AMI-WIND RA	100 km 500 km 3-5 km	25m 50 km 7 km	From 1995
RADARSAT	Synthetic Aperture Radar	SAR	max. 500 km	28m / 50m / 100m	From 1995
QuickScat	Wind scatterometer	SeaWinds	1800 km	25 km	From 1999
TOPEX-Poseidon	Altimeters	T/P	NA	6 km	From 1992
GFO	GEOSAT follow-on altimeter	RA	NA	5 - 10 km	From 1998

NA: not applicable

Future

Satellite	Instrument	Acronym	Swath width	Spatial Resolution	Launch
VNIR only					
ENVISAT	Medium Resolution Imaging Spectrometer	MERIS	1150 km	300m / 1200m	2001
ADEOS-2	Polarization and Directionality of the Earth's Reflectance	POLDER-2	2400km	6km	2000
ADEOS-3	Super Global Imager	S-GLI (OCI)	1600 km	1km	2004
VNIR and TIR					
ADEOS-2	Global Imager	GLI	1600 km	250m – 1km	2000
NOAA-POES series	Advanced Very High Resolution Radiometer	AVHRR/3	3000 km	1 km	2001
METOP	Advanced Very High Resolution Radiometer	AVHRR/3	3000 km	1 km	2002
ENVISAT	Advanced Along Track Scanning Radiometer	AATSR (TIR)	500 km	1 km	2001
EOS-PM1	MODIS	MODIS	2330	1 km	2001
NOAA-GOES GOES-L - M	Visible and IR Spin-Scan Radiometer	VISSR	Full Earth disc*	7, 14 km	2000
MSG	Meteosat second generation	SEVIRI	Full Earth disk*	5 km	2003
PWM					
ADEOS-2	Advanced Microwave Scanning Radiometer	AMSR	1450 km	5 - 50 km	2000
NPOESS	Passive microwave polarimetry	WindSat	1025 km	25 km	2002
SMOS	L-band microwave radiometer	SMOS	1200 km	50 km	2005
AMW					
ENVISAT	Advanced SAR RA-2	ASAR RA-2	Max. 420 km	30m / 150m / 1km 7 km	2001
RADARSAT2	Synthetic Aperture Radar	SAR	Max. 500 km	28m / 50m / 100m	2001
ALOS	Phased array type L-band SAR	PALSAR	250 – 350 km	100 m	2003
ADEOS-2	Scatterometer	SeaWinds	1800 km	50 km	2000
METOP	Advanced Wind Scatterometer	ASCAT	1000 km	25 km	2003
JASON	Altimeter	Jason	NA	6 km	2000
ICESAT	Laser altimeter	GLAS	NA	250 m	2002
CRYOSAT	Radar altimeter	-	NA	400 m	2003

*: Swath width for geostationary satellite is indicated as full Earth disc.
NA: not applicable

Tables and Captions

Parameter	Measurement Principals				
	VNIR	TIR	PMW	AMW	
				Side-looking	Nadir
Sea ice extent	**C,R**		**C,OP,R**	**C,OP,R**	
Sea ice concentration & type			**C,OP,R**	**C,OP,R**	
Sea ice edge features	**R**		**C,OP,R**	**C,OP,R**	
Sea ice motion			**C,OP,R**	**C,OP,R**	
Sea surface temperature		**C,OP,R**	**R**		
Wave spectra				**C,OP,R**	
Significant waveheight					**C,OP,R**
Vector wind				**C,OP,R**	
Wind speed			**R**	**R**	**C,OP,R**
Current fronts & eddies		**R**		**R**	**C,OP,R**
Internal waves				**R**	
Sea Level					**C,OP,R**
Surface geostrophic current					**C,OP,R**
Shallow water bathymetry	**OP, R**			**OP,R**	
Surface slicks (oil spill, film)	**R**			**OP,R**	
Clorophyll concentration	**OP,R**			**R**	
Primary Production	**R, C**				

Table 1. Overview of surface parameters derived from satellite based Earth Observation. The classes are: C - climate monitoring, OP - operational, and R – research. Not included in the table are atmospheric quantities such as column-integrated water vapor and liquid water derived by passive microwave observations.

Satellite	Operation dates	Split-channel
TIROS-N	Oct. 78 -Jan. 80	No
NOAA-6	Jun. 79 -Mar. 83	No
NOAA-7	Aug. 81 - Feb. 85	Yes
NOAA-8	May. 83 -Oct. 85	No
NOAA-9	Feb. 85 - Nov. 88	Yes
NOAA-10	Nov. 86 - Sep. 91	No
NOAA-11	Nov. 88 - Apr. 95	Yes
NOAA-12	Sep. 91 - present	Yes
NOAA-14	Dec. 94 - present	Yes

Table 2. TIROS -NOAA satellites carrying AVHRR sensors.

PROCESSES	PARAMETERS		
	Ice Mass	Sea Surface Salinity	Marine Geoid
Thermohaline Circulation	ICESat, Cryosat	SMOS	GOCE, (GRACE)
Sea Level Change	ICESat, Cryosat, GRACE, GOCE		GOCE,
Air-Sea-Ice Interaction (+ albedo effect)	ICESat, Cryosat		
Evaporation minus Precipitation		SMOS, + TRMM follow-on	
Mass and Heat Transport		(SMOS)	GOCE, (GRACE)
Large Scale Frontal Dynamics		SMOS	GOCE
Evolution of Large Scale Salinity Event	(ICESat, Cryosat)	SMOS, +TRMM follow-on	

Table 3. Connection between the three geophysical quantities, the oceanic processes that in different ways are contributing to climate and the candidate satellite missions.

Figure captions

Figure 1. The electromagnetic (EM) spectrum showing the bands used in remote sensing together with the operating area for some sensors (upper graph). The atmospheric transmission of the EM spectrum is shown in the lower graph. Note that the operating areas for satellite oceanography are located in parts of the spectrum where atmospheric transmission is high.

Figure 2. Maps of maximum and minimum sea ice extent and concentration in the Arctic and Antarctic obtained from passive microwave satellite data from the Special Sensor Microwave Imager (SSM/I) operated on the Defense Meteorological Satellite Program (DMSP) (after Bjørgo *et al.*, 1997). The maps are from March 1993 (upper left and lower left figure) and September 1993 (upper right and lower right figure). Copyright American Geophysical Union. Ice concentrations, indicated by the colour bar with 100% in white, 15% in light blue and no ice in blue, were computed from SSM/I data using the Norwegian NORSEX algorithm (after Svendsen *et al*., 1983). Note that the two filled circles over the central Arctic marks the data-gap.

Figure 3. Microwave emissivity as a function of frequency and polarisation for open water, first year and multiyear ice, measured during the NORSEX experiment in 1979 (after Svendsen *et al*., 1983). Two curves are provided for each of the three classes as defined by the vertical (V-pol) and horizontal (H-pol) polarisation. Note that the spatial orientation of the electric (and magnetic) fields of an electromagnetic wave versus the surface of the medium that the wave is incident upon is normal for V-pol and parallel for H-pol. Copyright American Geophysical Union.

Figure 4. Time series of Arctic ice area derived from Nimbus-7 SMMR and DMSP SSM/I satellite passive microwave data: (a) is monthly mean and (b) area anomalies from 1978-95 where the linear regression indicates a ~31,000 km^2 yr^{-1} decrease, corresponding to ~3% per decade

(Bjørgo *et al*. 1997). (c) is the fraction of multi-year (i.e., having survived the summer melt) sea ice area in winter (November-March), 1978-98, where the linear regression indicates a ~30,000 km^2 yr^{-1} decrease, corresponding to ~7% per decade (after Johannessen *et al*., 1999).

Figure 5. Monthly mean sea surface temperature (SST) differences between July 1995 and July 1997 derived from ERS-2 Along Track Scanning Radiometer (ATSR). Clearly noticed is the SST Expression of the 1997 El Niño with a sea surface temperature anomaly (the colour code is given in degrees Celsius with blue equal - 3˚ C). Acknowledgement ESA-ESRIN.

Figure 6. Global map of eight days of the PODAAC data showing the sea surface temperature distribution of warm equatorial and tropical waters (brown-yellow), extra-tropical and mid-latitude waters (yellow-green-blue) and the colder high latitude and polar waters (violet-pink). Acknowledgement NASA/JPL.

Figure 7. Global map of rms sea level variability (in centimeter height relative to the time-invariant mean surface) from ERS-1 Radar Altimeter obtained from cycles 6 to 18 (October 1992 to December 1993) after correction using TOPEX/POSEIDON precise orbit. The colour code represents height intervals from 2 cm (light yellow) to 25 cm (red). With the TOPEX/POSEIDON orbit as reference Traon and Oger (1998) calculated the ERS-1 orbit error to within about 2 cm rms. (Courtesy of P.-Y. Le Traon).

Figure 8. Sea surface topography anomaly ranging from about 30 to 10 cm (red-to-yellow colours) of the 1997 El Niño derived from the ERS-2 Radar Altimeter (Acknowledgement Delft Univ. of Technology/ESA-ESRIN).

Figure 9. Global seasonal distribution of photosynthetic pigments (chlorophyll and phaeophytin) as derived from the processing of the four first years of the CZCS data acquisition from November 1978 to October 1981. Panel (a) shows the averaged pigment distribution from March to May. Panel (b) displays the same information for June to August. Panel. Panel (c) is for September to November, and Panel (d) for the period covering December to February. Among other, the highly productive coastal upwelling off West-Africa is clealy oberved, as well as its seasonal variability, which is characterised by an increase of pigment concentration from spring to summer and a decrease in winter time. We clearly observe the variability of pigment concentration along the coast of Yemen and Oman, which can be related to the general moonson regime in the northern part of the Indian Ocean (Acknowledgement NASA/GSFC).

Figure 10. Seasonal averaged estimates of primary production using pigment concetration derived from the 1978-1981 CZCS data set and the so-called ”Vertically Generalized Production Model” obtained by Behrenfeld & Falkowski (1997). In particular, seasonal variability between the northern and the southern hemisphere are well reproduced (Courtesy of M.J. Behrenfeld and P.G. Falkowski). Copyright American Society of Limnology & Oceanography.

Figure 11. Monthly mean sea ice motion vectors delivered from RGPS using SSM/I data. The solid lines indicate the mean surface pressure (units of millibar) in October 1997, while the arrows give the monthly averaged sea ice drift speed and direction scaled to the 25 km/day (25 cm/s) marker. Acknowledgement NASA/JPL.

Figure 12. Picture of Russian nuclear powered icebreaker “Sibiria” leading a convoy of cargo vessels sailing through 2 m thick firstyear ice in the Northern Sea Route (Courtesy Murmansk Shipping Company).

Figure 13. (a) Chlorophyll pigment concentration product from SeaWiFS over the North Sea and the Skagerrak on May 19th 1999 (© Orbital Imaging Corp. and NASA SeaWiFS project). (b) Sea surface temperature distribution as derived from NOAA-AVHRR for May 19th 1999 over the same region. These image data allow characterisation of the main water masses, circulation patterns and current fronts. One can observe the cool oligotrophic water coming from the Atlantic ocean into the North Sea and the Skagerrak Sea (in purple and blue). Warm waters from the Baltic (in red in the SST image) meet the cold waters in the Skagerak giving raise to turbulent processes, such as eddies. Along the western coast of Norway, the turbulent Norwegian current shows complex eddy circulation patterns, and is caharcterised by warm waters at this period of the year (13 –15^{o}), as well as somewhat high chlorpphyll concentration (up to 5 mg·m^{-3}). Data courtesy: Steve Groom, Centre for Coastal and Marine Sciences – Plymouth Marine Laboratory.

Figure 14. Chlorophyll pigment concentration as derived from processing of SeaWiFS ocean colour data for the North Sea and the Skagerrak, on (a) May 13, (b) May 15 and (c) May 17, 1998 (© Orbital Imaging Corp. and NASA SeaWiFS project). The time series shows the increases and demise of a *Chattonella spp*. bloom along the Danish coast, for the first time reported in this region of the European waters. The bloom of this toxic algae extended up to the Norwegian coast where intensive aquaculture of salmon is carried out, leading to the death of 350 tonnes of farmed salmon. Blue indicates low pigment; red indicates high concentration of pigment and thus of *Chattonella*. Black area over the sea indicate clouds or unprocessed pixels. Data courtesy: Remote Sensing Group, Centre for Coastal and Marine Sciences – Plymouth Marine Laboratory.

Figure 15. a) SAR image (left) and example of optimized SAR derived mesoscale wind field (right) with the use of high-resolution wind field model (HIRLAM). Courtesy of M. Portabella; b) RADARSAT ScanSAR wide images of the Labrador Sea, each showing mesoscale flow patterns, including synoptic and polar lows (after Vachon *et al.*, 2000). Each image covers roughly 500 km from left to right. Copyright Canadian Space Agency.

Figure 16. Manifestation of the Norwegian coastal current front off the west coast of Norway on October 3, 1992 in a NOAA-AVHRR 1-km resolution image of the sea surface temperature field (dark red is 14 ° C and purple is 12 ° C) acquired at 14:20 UTC (left) and a ERS-SAR 100-m resolution image of the surface roughness field acquired at 21:35 UTC (right) (after Johannessen *et al.*, 1989). Both images cover approximately the same 100 km by 300 km region. In the left image the land is masked with green color. © ESA/NERSC.

Figure 17. Key modules of an integrated Earth system model applicable to the global ocean observing system consisting of an observation module, an interpretation module and a modeling and assimilation module (after ESA SP-1227).

Figure A1. Timeline of the most common Earth-observation VNIR/TIR passive sensors operated in space from 1972, together with those approved and planned towards 2010. The term "VNIR/TIR passive sensor" makes reference to instruments measuring either the radiation in the visible, near infrared part of the solar electromagnetic spectrum, which is reflected at the surface of the Earth (VNIR) or the radiation emitted by the Earth in the thermal infrared (TIR). VNIR sensors are used to derive biogeochemical parameters in the ocean upper layer, such as the concentration of chlorophyll pigments and suspended sediment. TIR instruments are mainly used to derive sea surface temperature.

Figure A2. Timeline of the most common Earth-observation microwave sensors operated in space from 1978, together with those approved and planned towards 2010. The term "passive microwave sensors" makes reference to instruments that measure the microwave radiation emitted by the Earth (PMW). The term "active microwave sensors" refers to instruments transmitting a source of electromagnetic energy towards the Earth and measuring the portion of the signal that is scattered back to antenna (AMW). Active microwave sensors usually include three main types of instruments: scatterometers from which the wind field over the ocean can be derived, imaging synthetic aperture radars – SAR that give access to a number of physical processes and phenomena at the surface of the sea (current front, waves, wind, etc.), and altimeters from which the sea-surface height can be estimated in addition to significant wave-height and wind speed.

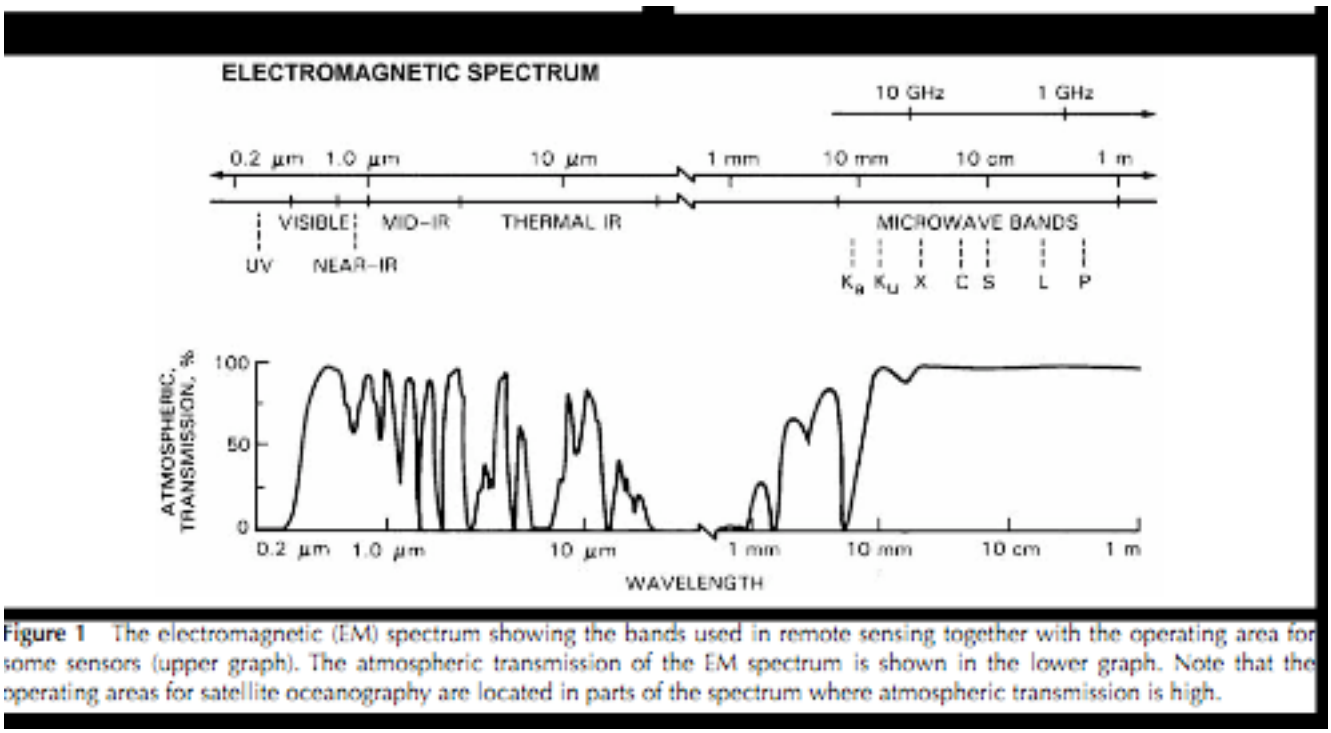

Figure 1 The electromagnetic (EM) spectrum showing the bands used in remote sensing together with the operating area for some sensors (upper graph). The atmospheric transmission of the EM spectrum is shown in the lower graph. Note that the operating areas for satellite oceanography are located in parts of the spectrum where atmospheric transmission is high.

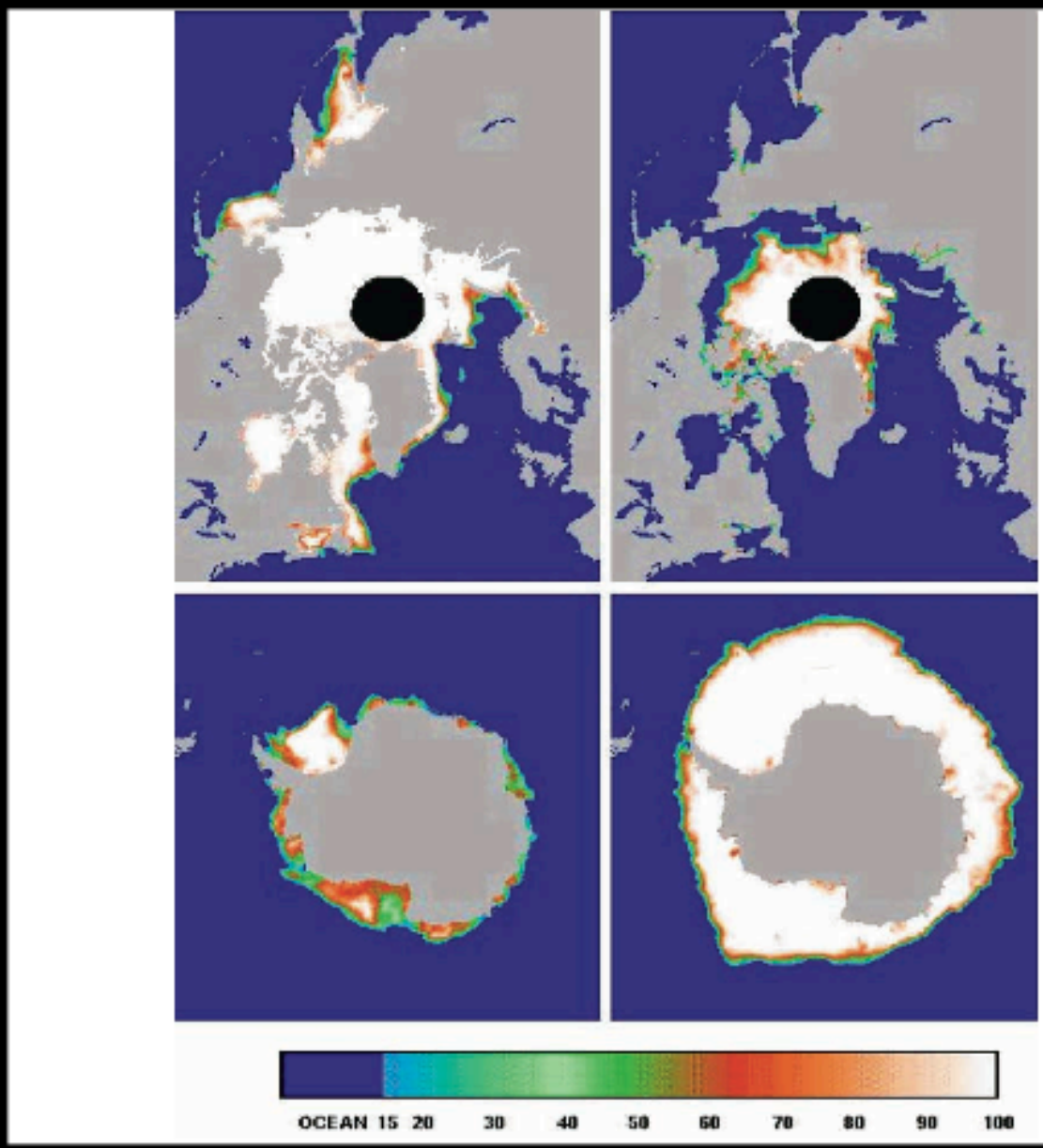

Figure 2 Maps of maximum and minimum sea ice extent and concentration in the Arctic and Antarctic obtained from passive microwave satellite data from the Special Sensor Microwave Imager (SSM/I) operated on the Defense Meteorological Satellite Program (DMSP) (after Bjørgo *et al.*, 1997). The maps are from March 1993 (upper left and lower left figure) and September 1993 (upper right and lower right figure). Copyright American Geophysical Union. Ice concentrations, indicated by the colour bar with 100% in white, 15% in light blue and no ice in blue, were computed from SSM/I data using the Norwegian NORSEX algorithm (after Svendsen *et al.*, 1983). Note that the two filled circles over the central Arctic marks the data-gap.

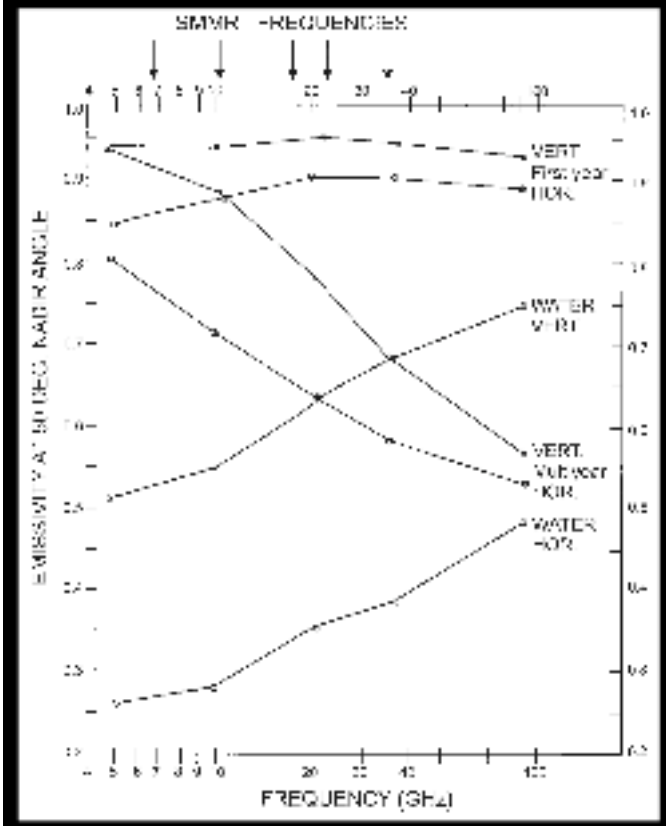

Figure 3 Microwave emissivity as a function of frequency and polarisation for open water, first year and multiyear ice, measured during the NORSEX experiment in 1979 (after Svendsen *et al.*, 1983). Two curves are provided for each of the three classes as defined by the vertical (V-pol) and horizontal (H-pol) polarisation. Note that the spatial orientation of the electric (and magnetic) fields of an electromagnetic wave versus the surface of the medium that the wave is incident upon is normal for V-pol and parallel for H-pol. Copyright American Geophysical Union.

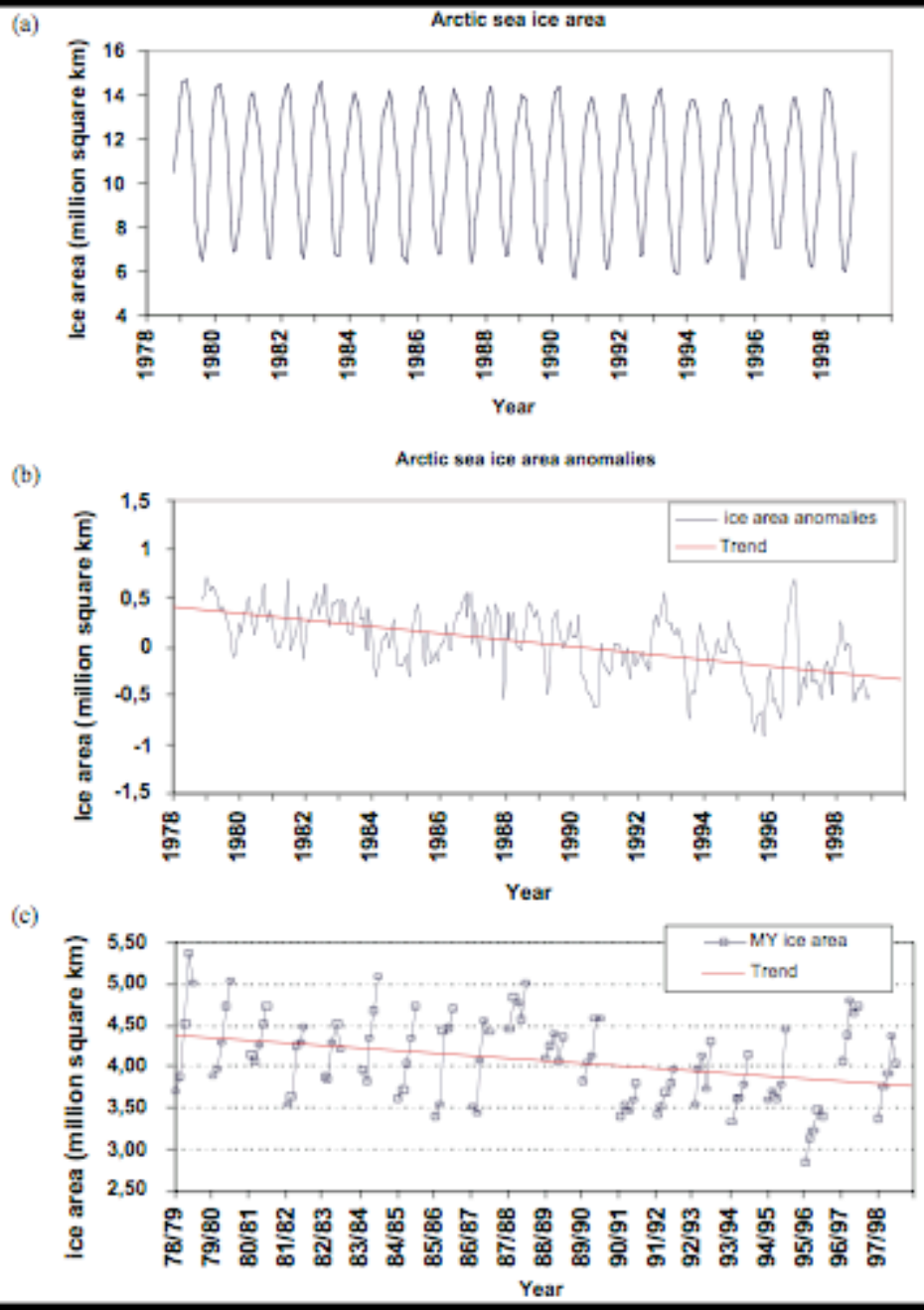

Figure 4 Time series of Arctic ice area derived from Nimbus-7 SMMR and DMSP SSM/I satellite passive microwave data: (a) is monthly mean and (b) area anomalies from 1978–98 where the linear regression indicates a ~31,000 $km^2 yr^{-1}$ decrease, corresponding to ~3% per decade (Bjørgo *et al.*, 1997). (c) is the fraction of multi-year (i.e., having survived the summer melt) sea ice area in winter (November – March), 1978–98, where the linear regression indicates a ~30,000 $km^2 yr^{-1}$ decrease, corresponding to ~7% per decade (after Johannessen *et al.*, 1999). (Copyright 2000 American Association for the Advancement of Science.

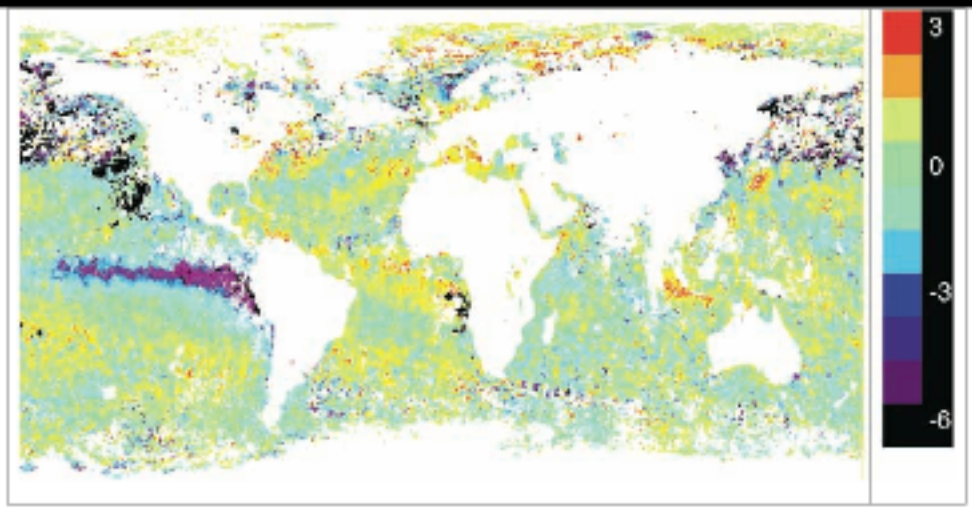

Figure 5 Monthly mean sea surface temperature (SST) differences between July 1995 and July 1997 derived from ERS-2 Along Track Scanning Radiometer (ATSR). Clearly noticed is the SST Expression of the 1997 El Niño with a sea surface temperature anomaly (the colour code is given in degrees Celsius with blue equal −3 °C). (Acknowledgement ESA-ESRIN.)

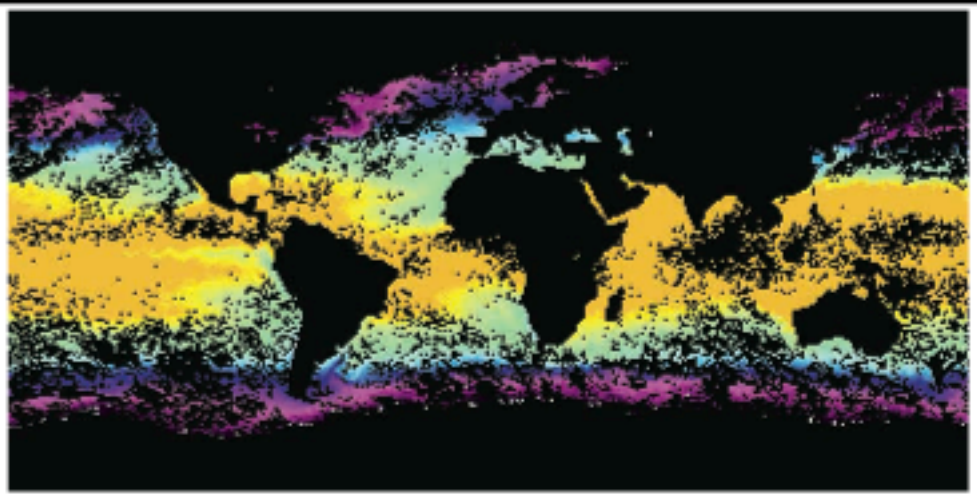

Figure 6 Global map of eight days of the PODAAC data showing the sea surface temperature distribution of warm equatorial and tropical waters (brown–yellow), extra-tropical and mid-latitude waters (yellow–green–blue) and the colder high latitude and polar waters (violet–pink). (Acknowledgement NASA/JPL.)

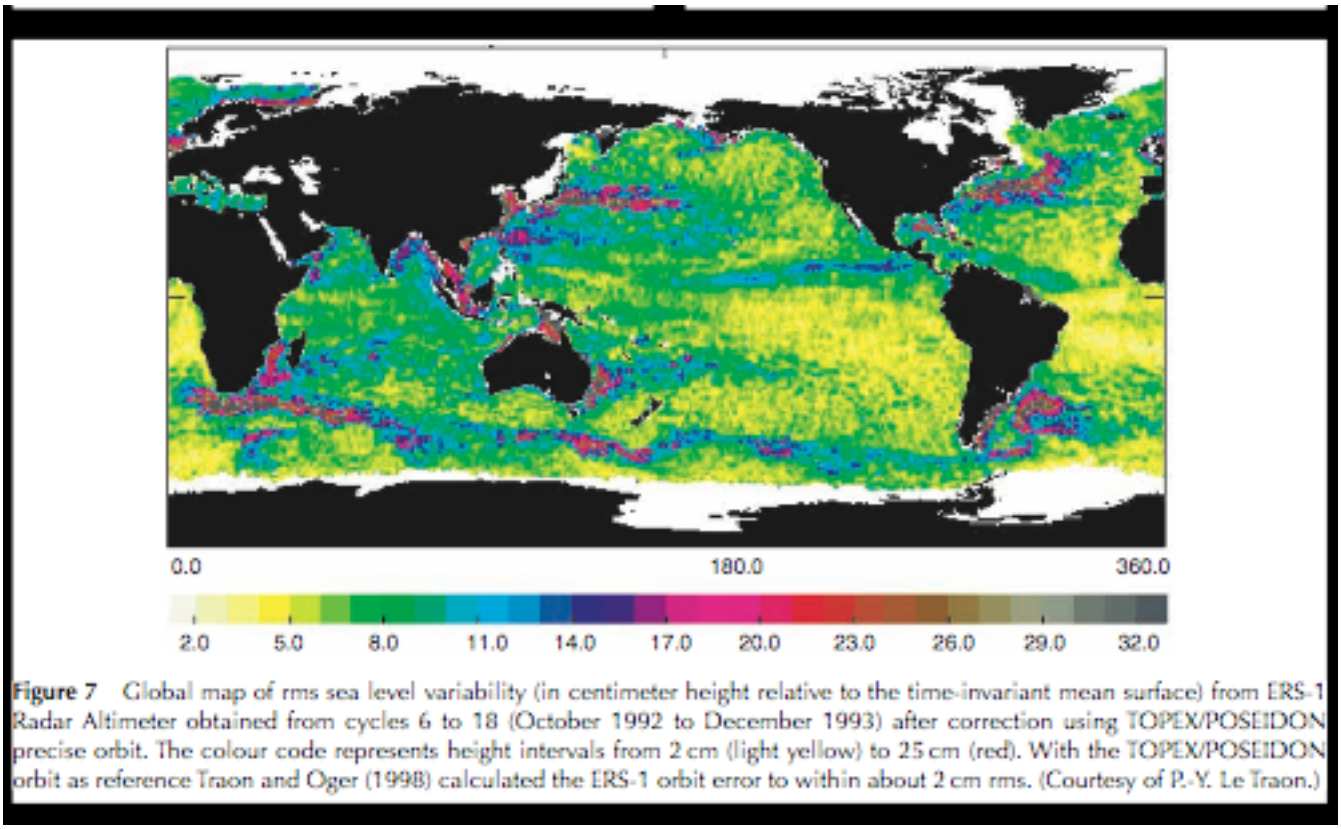

Figure 7 Global map of rms sea level variability (in centimeter height relative to the time-invariant mean surface) from ERS-1 Radar Altimeter obtained from cycles 6 to 18 (October 1992 to December 1993) after correction using TOPEX/POSEIDON precise orbit. The colour code represents height intervals from 2 cm (light yellow) to 25 cm (red). With the TOPEX/POSEIDON orbit as reference Traon and Oger (1998) calculated the ERS-1 orbit error to within about 2 cm rms. (Courtesy of P.-Y. Le Traon.)

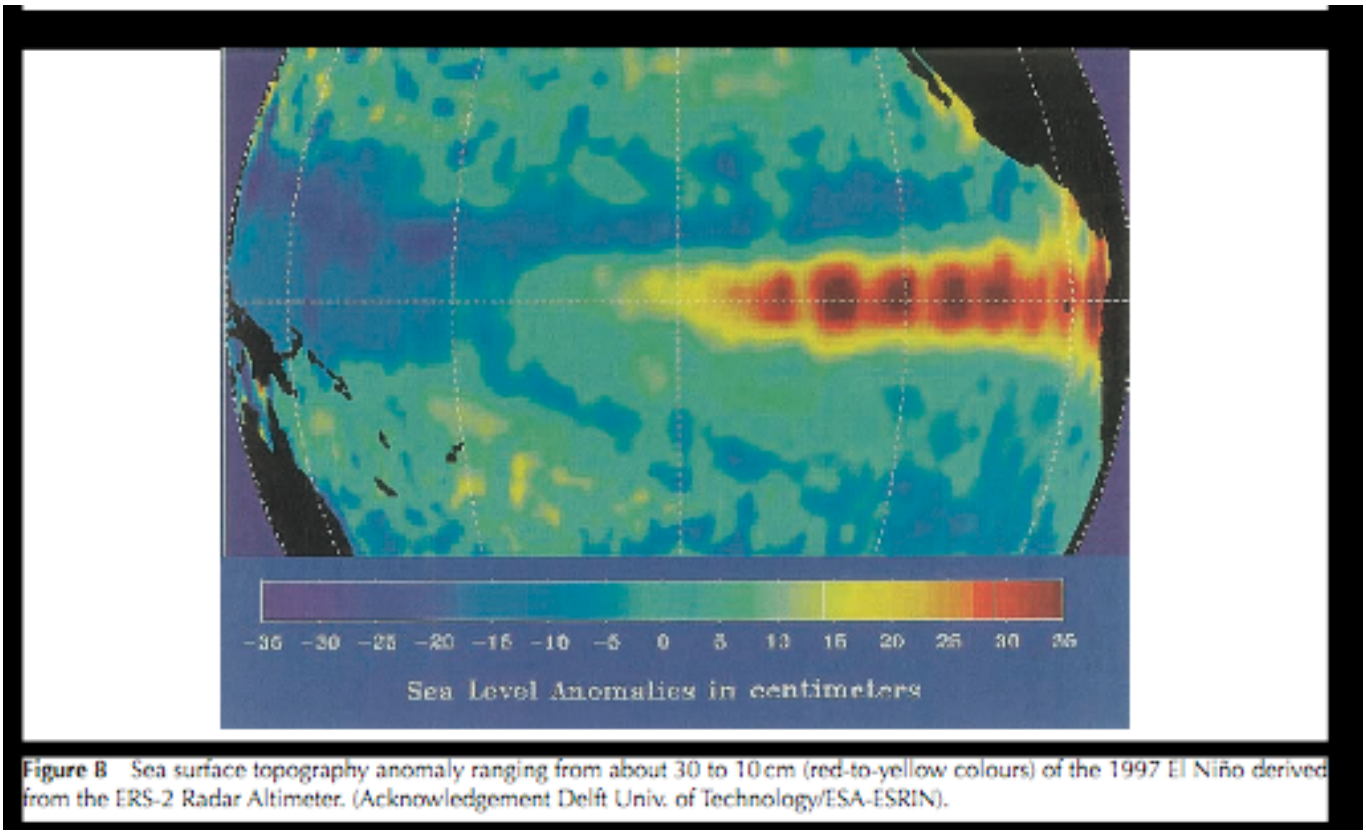

Figure 8 Sea surface topography anomaly ranging from about 30 to 10 cm (red-to-yellow colours) of the 1997 El Niño derived from the ERS-2 Radar Altimeter. (Acknowledgement Delft Univ. of Technology/ESA-ESRIN).

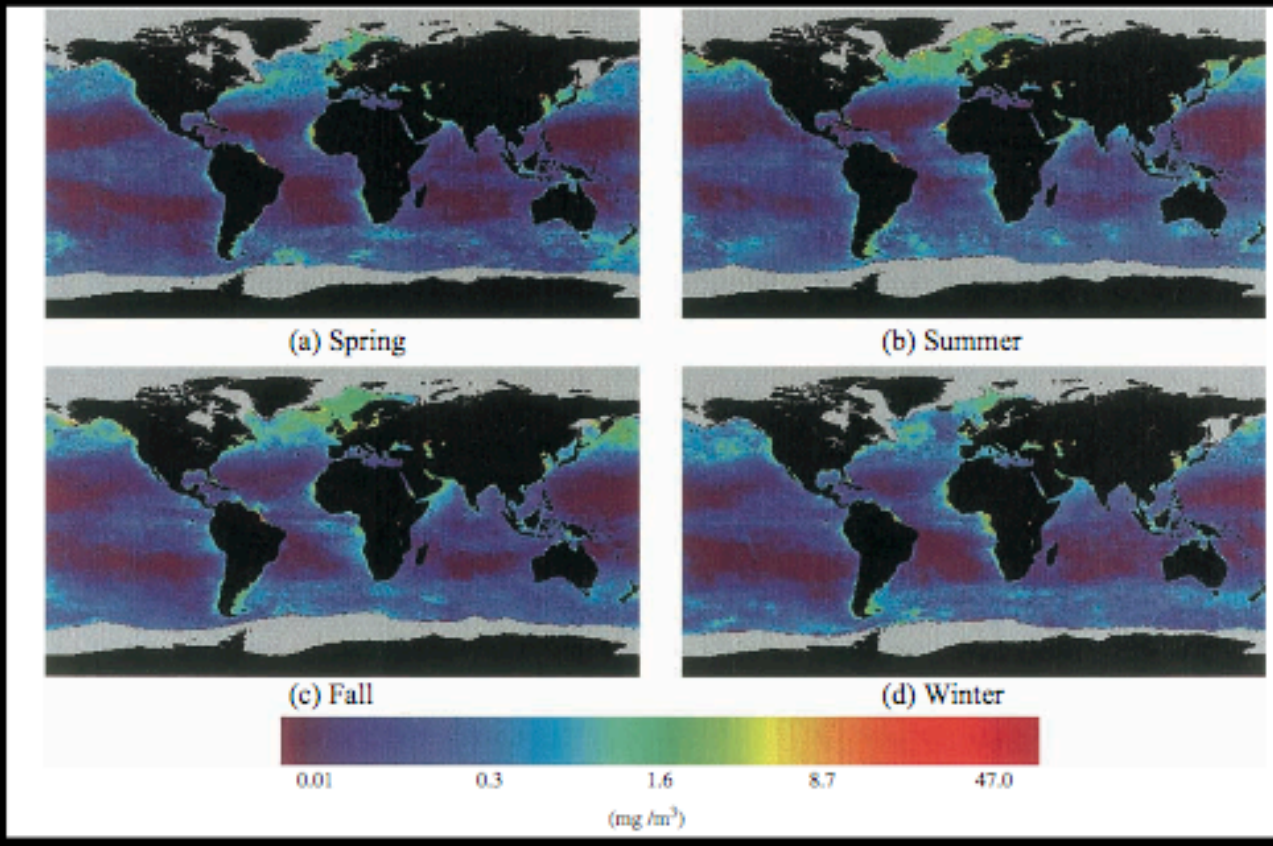

Figure 9 Global seasonal distribution of photosynthetic pigments (chlorophyll and phaeophytin) as derived from the processing of the four first years of the CZCS data acquisition from November 1978 to October 1981. Panel (a) shows the averaged pigment distribution from March to May. Panel (b) displays the same information for June to August. Panel (c) is for September to November, and Panel (d) for the period covering December to February. Among other, the highly productive coastal upwelling off West-Africa is clearly observed, as well as its seasonal variability, which is characterised by an increase of pigment concentration from spring to summer and a decrease in winter time. We clearly observe the variability of pigment concentration along the coast of Yemen and Oman, which can be related to the general moonson regime in the northern part of the Indian Ocean. (Acknowledgement NASA/GSFC.)

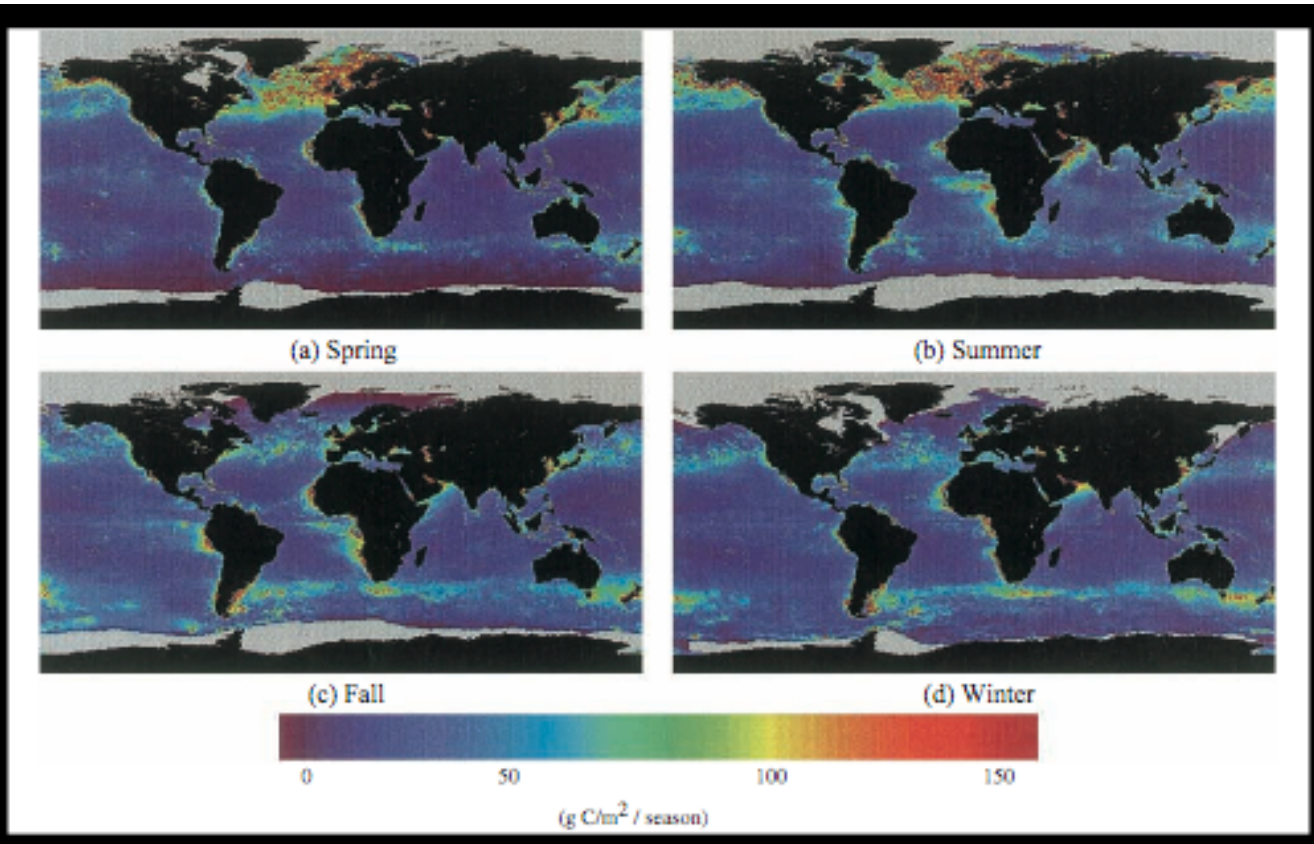

Figure 10 Seasonal averaged estimates of primary production using pigment concentration derived from the 1978–1981 CZCS data set and the so-called "Vertically Generalized Production Model" obtained by Behrenfeld and Falkowski (1997). In particular, seaonal variability between the northern and the southern hemisphere are well reproduced. (Courtesy of M.J. Behrenfeld and P.G. Falkowski; Copyright American Society of Limnology & Oceanography.)

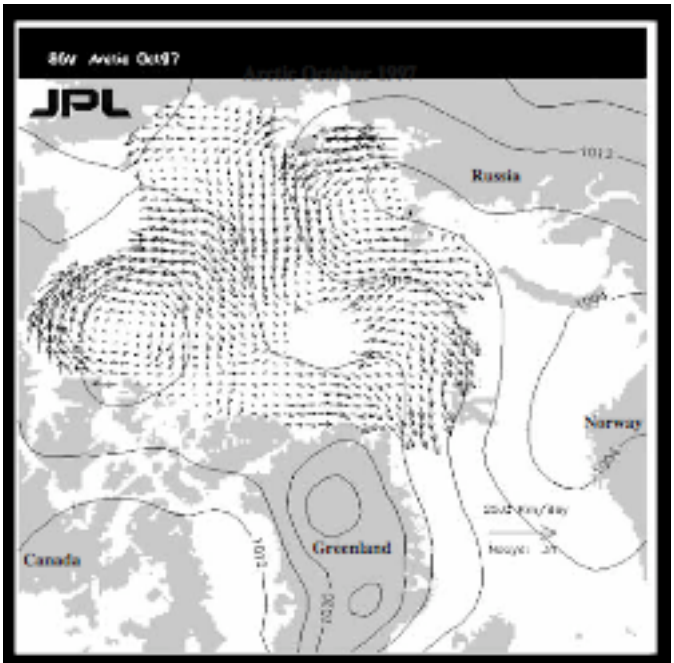

Figure 11 Monthly mean sea ice motion vectors delivered from RGPS using SSM/I data. The solid lines indicate the mean surface pressure (units of millibar) in October 1997, while the arrows give the monthly averaged sea ice drift speed and direction scaled to the 25 km/day (25 cm/s) marker. (Acknowledgement NASA/JPL.)

Figure 12 Picture of Russian nuclear powered icebreaker "Sibiria" leading a convoy of cargo vessels sailing through 2 m thick firstyear ice in the Northern Sea Route. (Courtesy Murmansk Shipping Company.)

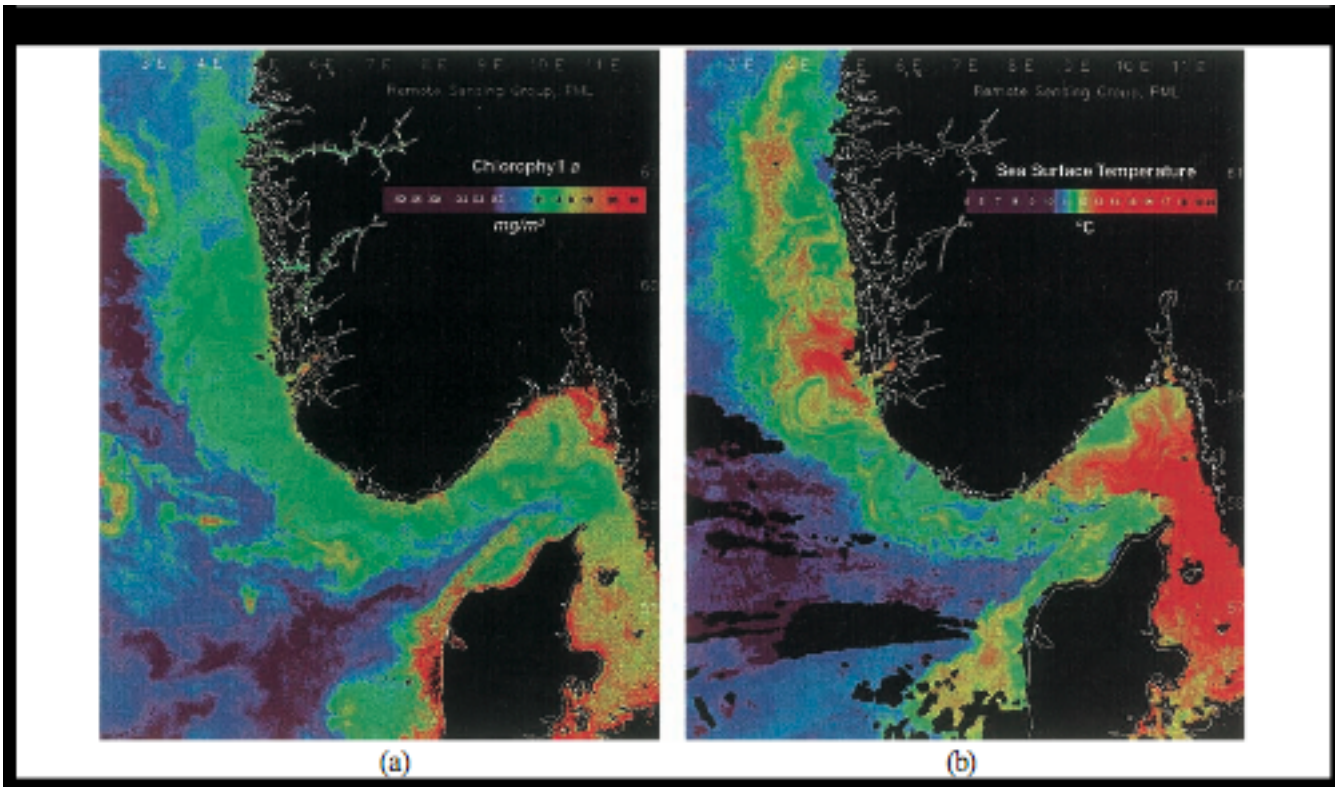

Figure 13 (a) Chlorophyll pigment concentration product from SeaWiFS over the North Sea and the Skagerrak on May 19th 1999 (© Orbital Imaging Corp. and NASA SeaWiFS project). (b) Sea surface temperature distribution as derived from NOAA-AVHRR for May 19th 1999 over the same region. These image data allow characterisation of the main water masses, circulation patterns and current fronts. One can observe the cool oligotrophic water coming from the Atlantic ocean into the North Sea and the Skagerrak Sea (in purple and blue). Warm waters from the Baltic (in red in the SST image) meet the cold waters in the Skagerak giving raise to turbulent processes, such as eddies. Along the western coast of Norway, the turbulent Norwegian current shows complex eddy circulation patterns, and is characterised by warm waters at this period of the year (13–15°), as well as somewhat high chlorophyll concentration (up to 5 $mg \cdot m^{-3}$). (Data courtesy: Steve Groom, Centre for Coastal and Marine Sciences – Plymouth Marine Laboratory.)

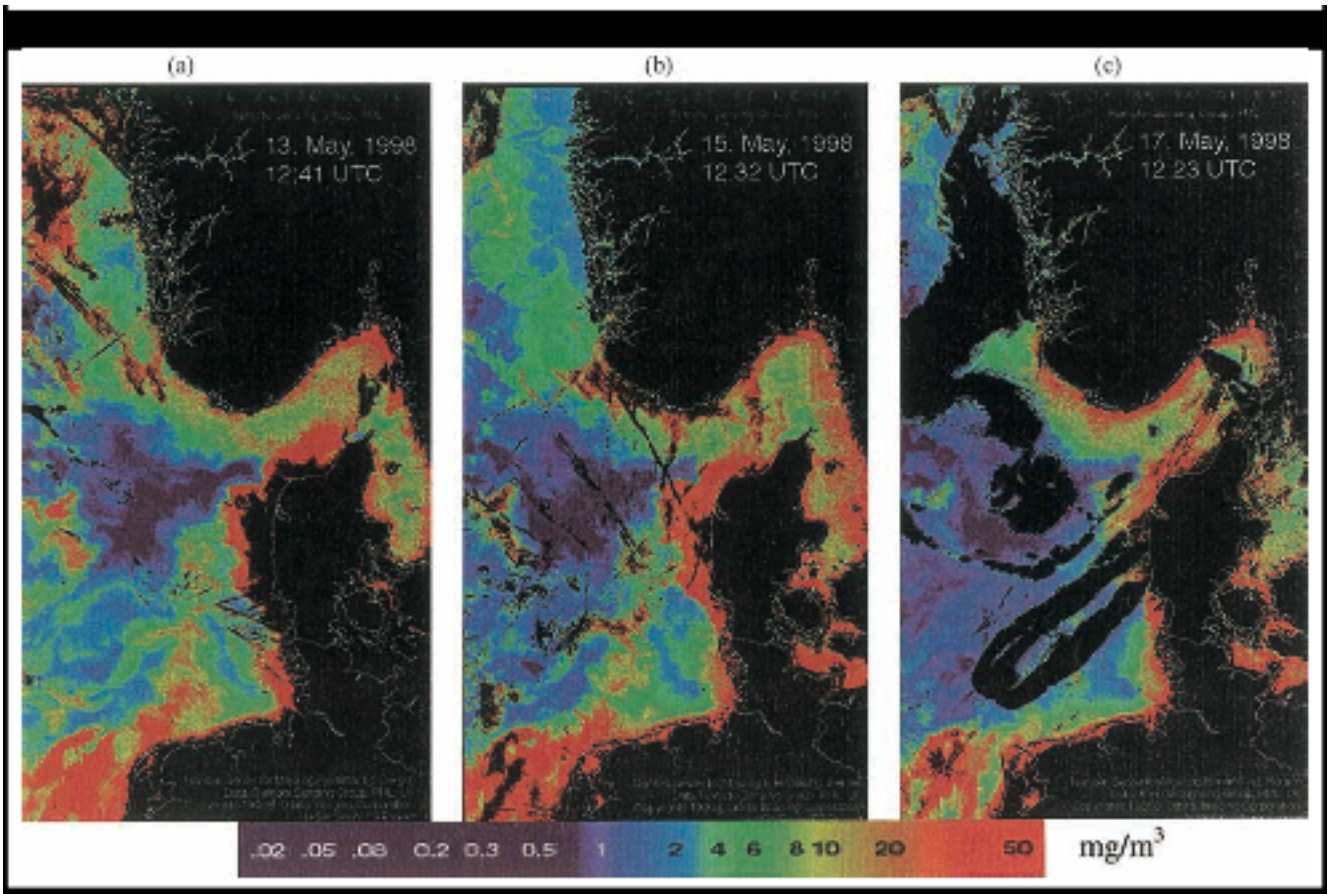

Figure 14 Chlorophyll pigment concentration as derived from processing of SeaWiFS ocean colour data for the North Sea and the Skagerrak, on (a) May 13, (b) May 15 and (c) May 17, 1998 (© Orbital Imaging Corp. and NASA SeaWiFS project). The time series shows the increases and demise of a *Chattonella* spp. bloom along the Danish coast, for the first time reported in this region of the European waters. The bloom of this toxic algae extended up to the Norwegian coast where intensive aquaculture of salmon is carried out, leading to the death of 350 tonnes of farmed salmon. Blue indicates low pigment; red indicates high concentration of pigment and thus of *Chattonella*. Black area over the sea indicate clouds or unprocessed pixels. (Data courtesy: Remote Sensing Group, Centre for Coastal and Marine Sciences – Plymouth Marine Laboratory.)

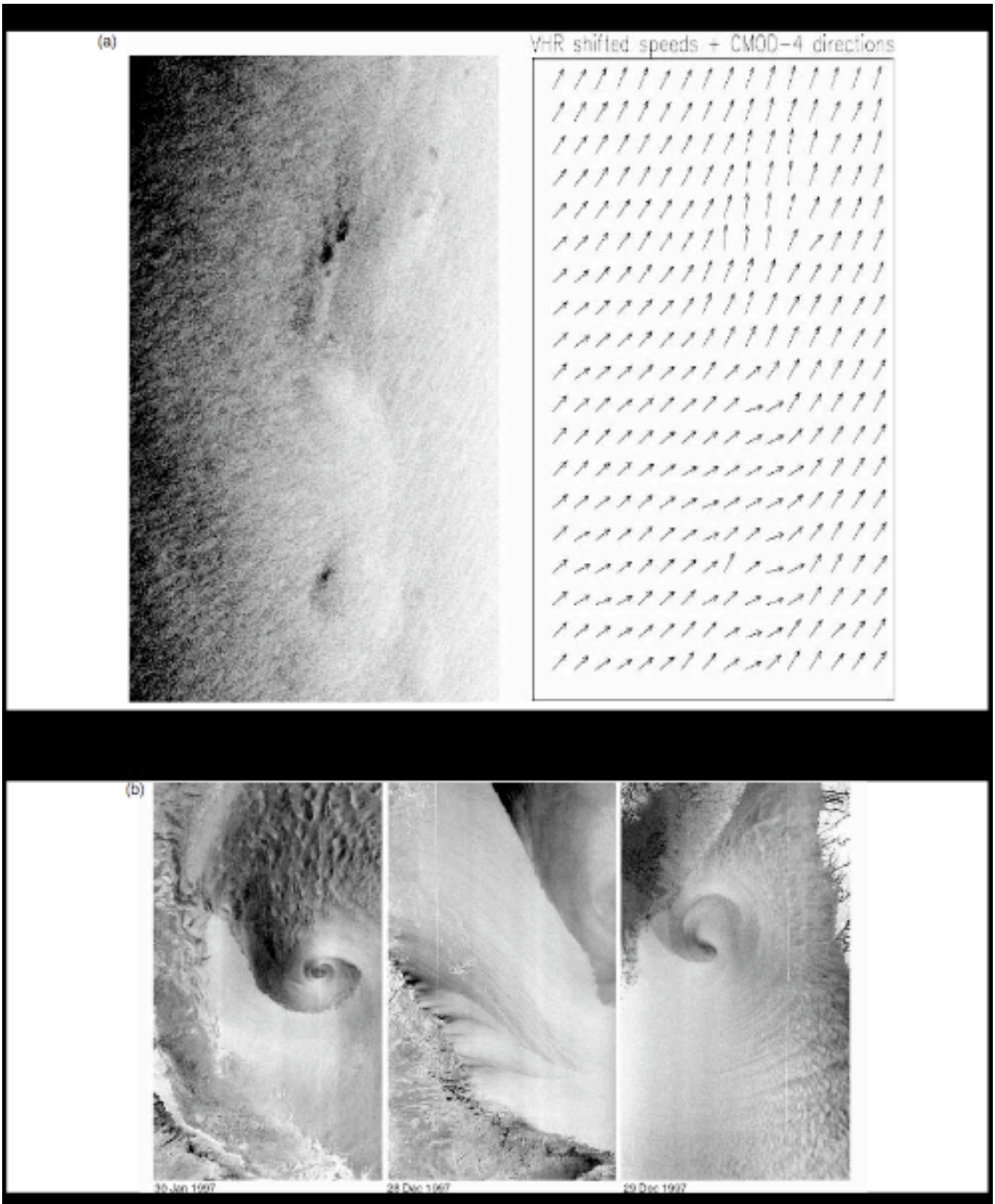

Figure 15 (a) SAR image (left) and example of optimized SAR derived mesoscale wind field (right) with the use of high-resolution wind field model (HIRLAM). Courtesy of M. Portabella; (b) RADARSAT ScanSAR wide images of the Labrador Sea, each showing mesoscale flow patterns, including synoptic and polar lows (after Vachon *et al.*, 2000). Each image covers roughly 500 km from left to right.

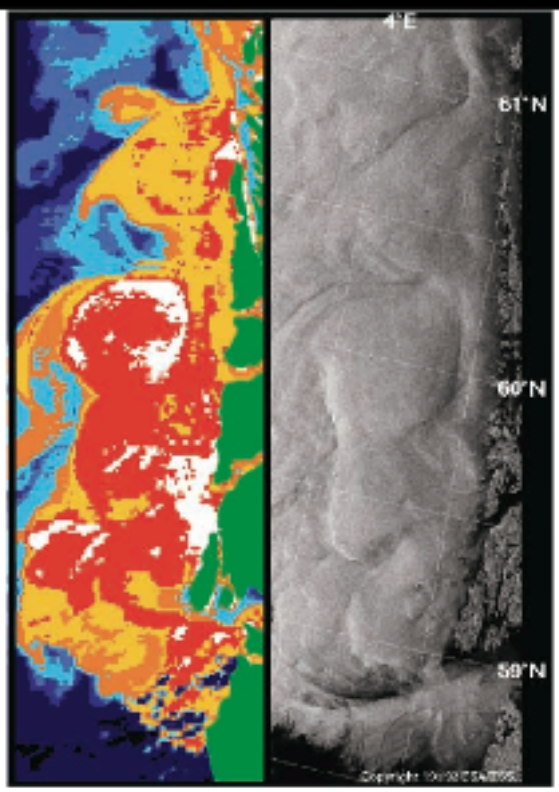

Figure 16 Manifestation of the Norwegian coastal current front off the west coast of Norway on October 3, 1992 in a NOAA-AVHRR 1-km resolution image of the sea surface temperature field (white is 14°C and dark blue is 12°C) acquired at 14:20 UTC (left) and a ERS-SAR 100-m resolution image of the surface roughness field acquired at 21:35 UTC (right) (after Johannessen *et al.*, 1989). Both images cover approximately the same 100 km by 300 km region. In the left image the land is masked with green color. (© ESA/NERSC.)

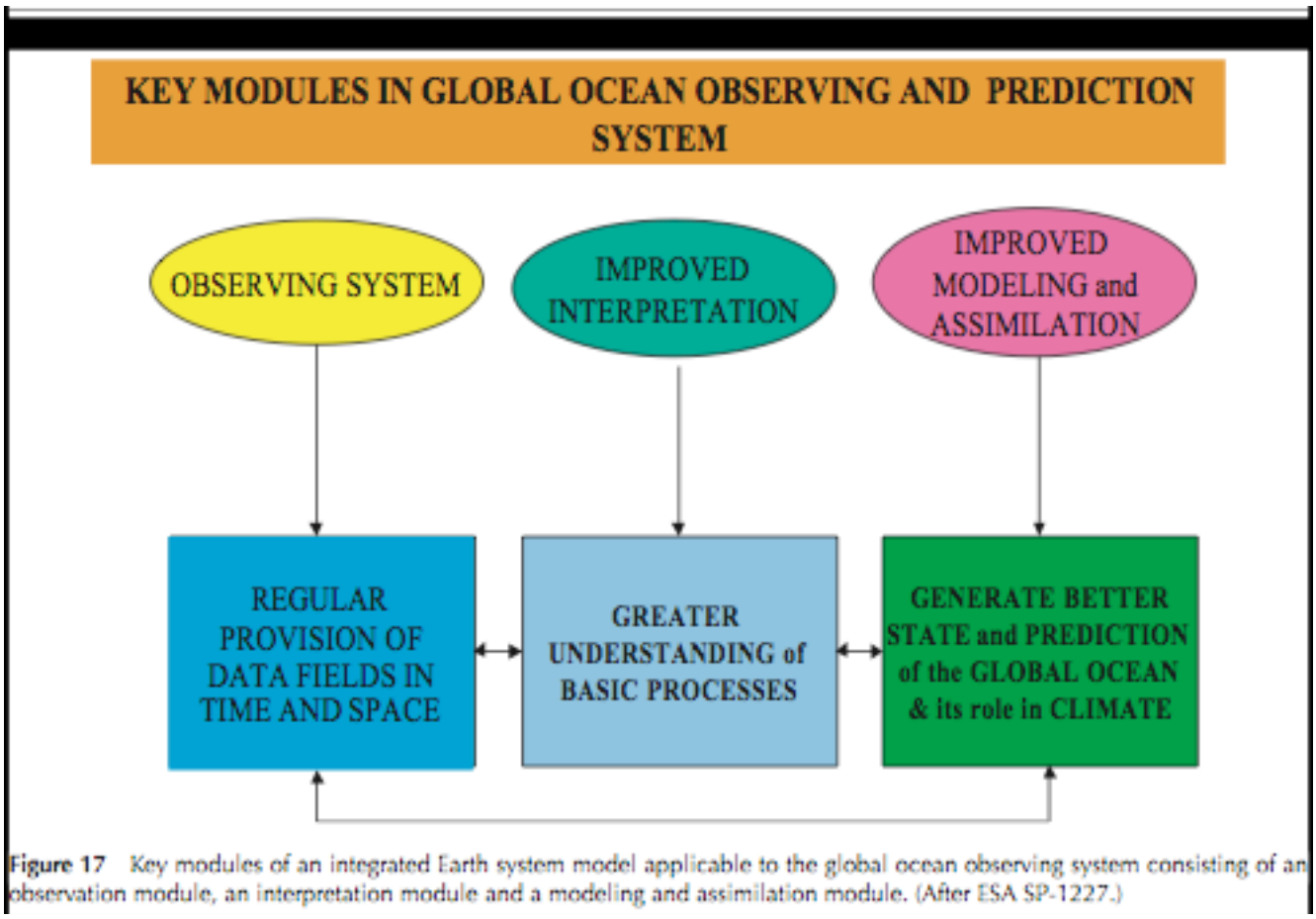

Figure 17 Key modules of an integrated Earth system model applicable to the global ocean observing system consisting of an observation module, an interpretation module and a modeling and assimilation module. (After ESA SP-1227.)

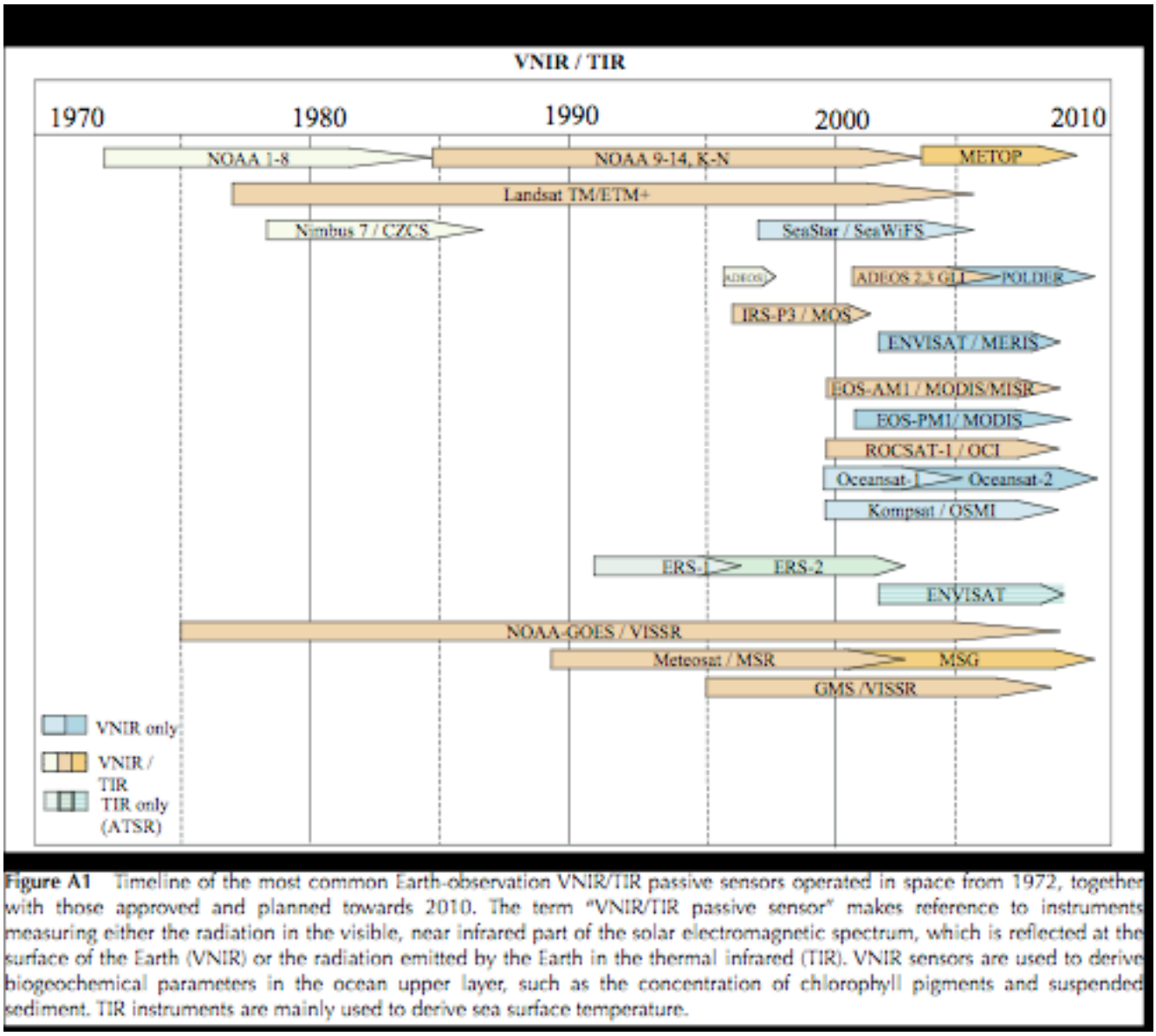

Figure A1 Timeline of the most common Earth-observation VNIR/TIR passive sensors operated in space from 1972, together with those approved and planned towards 2010. The term "VNIR/TIR passive sensor" makes reference to instruments measuring either the radiation in the visible, near infrared part of the solar electromagnetic spectrum, which is reflected at the surface of the Earth (VNIR) or the radiation emitted by the Earth in the thermal infrared (TIR). VNIR sensors are used to derive biogeochemical parameters in the ocean upper layer, such as the concentration of chlorophyll pigments and suspended sediment. TIR instruments are mainly used to derive sea surface temperature.

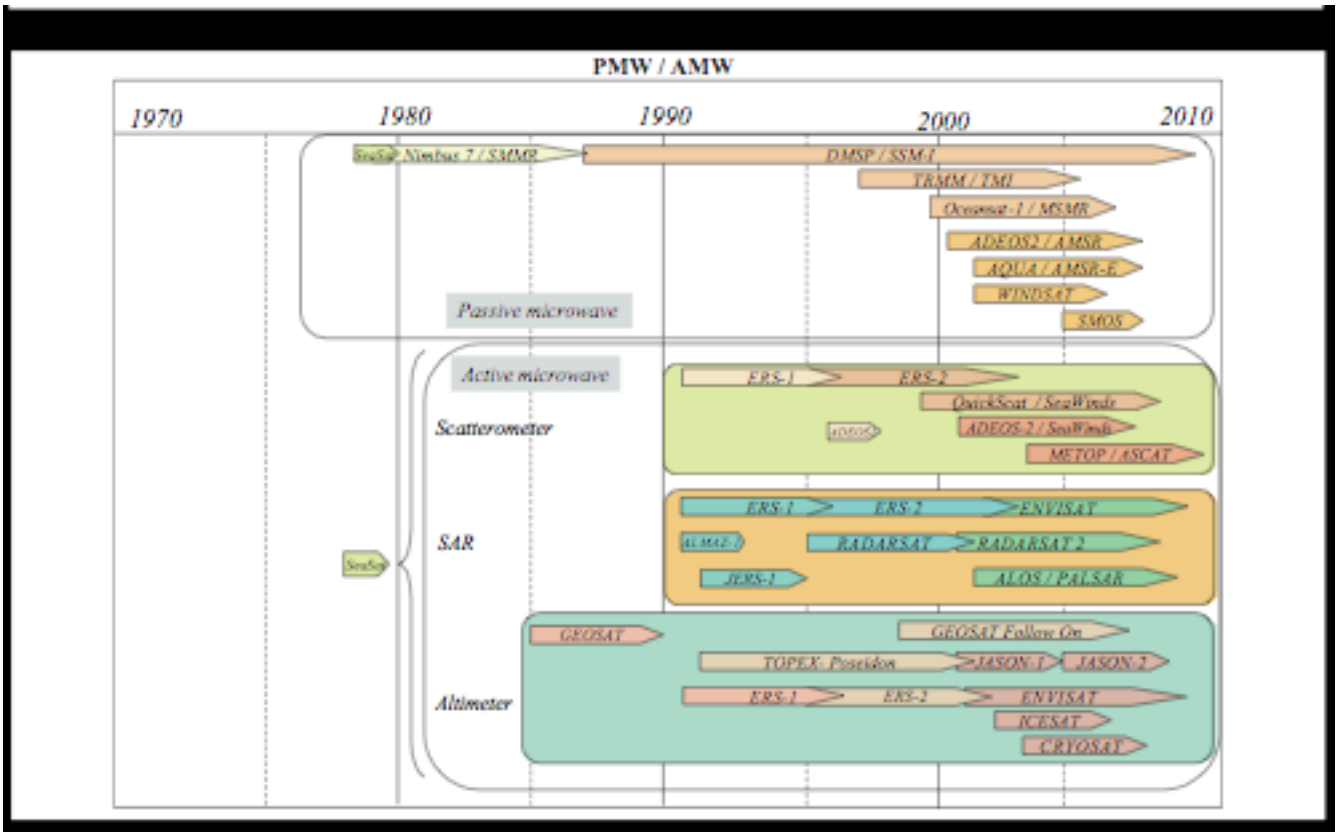

Figure A2 Timeline of the most common Earth-observation microwave sensors operated in space from 1978, together with those approved and planned towards 2010. The term "passive microwave sensors" makes reference to instruments that measure the microwave radiation emitted by the Earth (PMW). The term "active microwave sensors" refers to instruments transmitting a source of electromagnetic energy towards the Earth and measuring the portion of the signal that is scattered back to antenna (AMW). Active microwave sensors usually include three main types of instruments: scatterometers from which the wind field over the ocean can be derived, imaging synthetic aperture radars – SAR that give access to a number of physical processes and phenomena at the surface of the sea (current front, waves, wind, etc.), and altimeters from which the sea-surface height can be estimated in addition to significant wave-height and wind speed.